THESIS FOR THE DEGREE OF LICENTIATE OF ENGINEERING

Imidazolium ionic liquids nano-confined in mesoporous silica

Szilvia Vavra

Department of Chemistry and Chemical Engineering
Division of Applied Chemistry
CHALMERS UNIVERSITY OF TECHNOLOGY

Gothenburg, Sweden 2020

Imidazolium ionic liquids nano-confined in mesoporous silica
SZILVIA VAVRA

Thesis for the degree of Licentiate of Engineering
Licentiatuppsatser vid Institutionen för kemi och kemiteknik Chalmers tekniska högskola.
Nr 2020:08

Division of Applied Chemistry
Department of Chemistry and Chemical Engineering
Chalmers University of Technology
SE-412 96 Gothenburg
Sweden
Telephone: +46 (0)31-772 1000

Cover
Transmission electron microscopic image of an ionic liquid-templated silica thin film.

Printed by Chalmers Reproservice
Gothenburg, Sweden 2020

Imidazolium ionic liquids nano-confined in mesoporous silica
Thesis for the degree of Licentiate of Engineering
SZILVIA VAVRA

Department of Chemistry and Chemical Engineering
Division of Applied Chemistry
Chalmers University of Technology

Abstract

Protic ionic liquids (PILs), showing unique proton conductive properties, are considered to be suitable electrolytes for low and intermediate temperature fuel cells. To form solid-like electrolyte, one approach is to confine PILs in the pores of a solid matrix, thus forming a functional hybrid material in which the PIL constitutes a proton conductive phase and the matrix ensures mechanical stability.

In this work, proton transport mechanisms and correlated local structures in the binary liquid mixture of HC_8ImTFSI (1-octylimidazolium bis(trifluromethanesulfonyl)imide) and imidazole was studied while nano-confined in hydrophobized silica pores. For this, series of hybrid materials with varying liquid-to-silica ratios were investigated. One aspect considered in this approach was the effect of downsizing the pores on transport and structural properties. In these materials proton conduction properties were characterized by impedance spectroscopy and PFG NMR (pulse-field gradient nuclear magnetic resonance spectroscopy), under the assumption that the flipped-ion effect occurs, when the alkyl chains of the cations are oriented towards the hydrophobic silica pore walls. In such structuration, there are weak cation-pore wall interactions that favor unrestricted diffusion.

Ionic liquids (ILs) are also extremely interesting as multi-functional soft-templates for the synthesis of mesoporous materials and IL-based functional hybrid materials. Here, C_{16}MIMCl (1-hexadecyl-3-methylimidazolium chloride), was used as soft-template for the formation of vertically aligned, uniform, channel-like pores, running through the entire thickness of the film, with a well defined pore width of 2.5 nm in silica thin films deposited with the electrochemically assisted self-assembly (EASA) method. Furthermore, the mechanism of pore formation is explained; unlike the mechanisms reported for short chain imidazolium IL templates, in the case of C_{16}MIMCl the dominating so-called cooperative interaction is the electrostatic attraction between the $C_{16}MIM^+$ cation and the network-forming negatively charged silicate oligomers.

Keywords: oriented nanochannel, surface active ionic liquid (SAIL), protic ionic liquid, nano-confinement

List of publications

This thesis is based on the following appended papers

Paper I:
Transport properties and local structure of an imidazole/protic ionic liquid mixture confined in mesopores of hydrophobic silica
Szilvia Vavra, Khalid Elamin, Lars Nordstierna, and Anna Martinelli
Manuscript

Paper II:
An imidazolium ionic liquid as effective structure-directing agent for the fabrication of silica thin films with vertically aligned nanochannels
Szilvia Vavra, Neus Vila, Antiope Lotsari, Alain Walcarius, and Anna Martinelli
Submitted and under revision

My contribution

Paper I.:
I prepared the samples and carried out characterization with SEM, nitrogen adsorption, Infrared, SAXS, and jointly Raman spectroscopy. I performed data analysis and interpretation together with co-authors. I co-wrote the manuscript.

Paper II.:
I ideated the work and designed the experiments. I carried out the material synthesis and characterization with GISAXS, Infrared, SEM, and cyclic voltammetry (CV). I performed data analysis and interpretation in cooperation with co-authors. I wrote the first draft of the manuscript.

List of figures

Contents

1 Introduction

The hydrogen fuel cell technology has started to find its place in current and future energy systems and it can be said in an informal way that it is having its renaissance. There is an increased interest from industry that is also shown in the increasing amounts of commercially available applications using hydrogen fuel cells (e.g. in transportation and portable devices). Along with this trend, related research activity has been growing again for the last decade. Undoubtedly, hydrogen fuel cell technology has its key advantages: zero emission at point of use and ability to balance long-term intermittency in electricity generation [1]. Among other features, these give hydrogen-based energy systems an important role in realising decarbonisation of global energy systems in the near-future.

A fundamental aspect of the hydrogen fuel cell development is minimising losses that result in decreased cell potential. The actual cell potential is equal to the equilibrium potential (which gives the theoretical upper limit of 1.23 V under standard condition), reduced by the potential loss that is a sum of different types of losses [2]. The potential loss is shown by location on the cross-section of the cell in Fig. 1.1. Relevant contribution in the net potential loss comes from the ohmic (or resistive) loss of the proton conductive membrane. Thus, proton conductive materials are often studied also in the aspect of applicability in hydrogen fuel cell membranes. The need for suitable proton conductors for the next-generation of PEMs (proton exchange membranes) is especially high for use in low and intermediate temperature fuel cells, ideally operating above 120 °C and at anhydrous conditions (as established electrolytes exist for operation above 500 °C).[2–4]

Protic ionic liquids (PILs) are considered to be suitable electrolytes for low and intermediate temperature fuel cells operating up to 300 °C [3, 5–12]. Since fuel cells require a solid-like electrolyte to operate, a common approach is to confine PILs in the pores of a solid matrix, thus forming a functional hybrid material, in which the ionic liquid constitutes a proton conductive phase while the matrix ensures suitable mechanical properties [3, 5–7, 10, 11, 13].

The scope of this thesis is dual. In one aspect, the effect of nano-confinement on the desired physical and chemical properties of an imidazolium PIL was investigated. In an other approach, electrochemically assisted self-assembly (EASA) method was used to obtain mesoporous silica films in which an imidazolium ionic liquid formed orthogonally aligned ordered nanochannels. Hence, the future scope is to merge the two pathways by implementing EASA to protic ionic liquids.

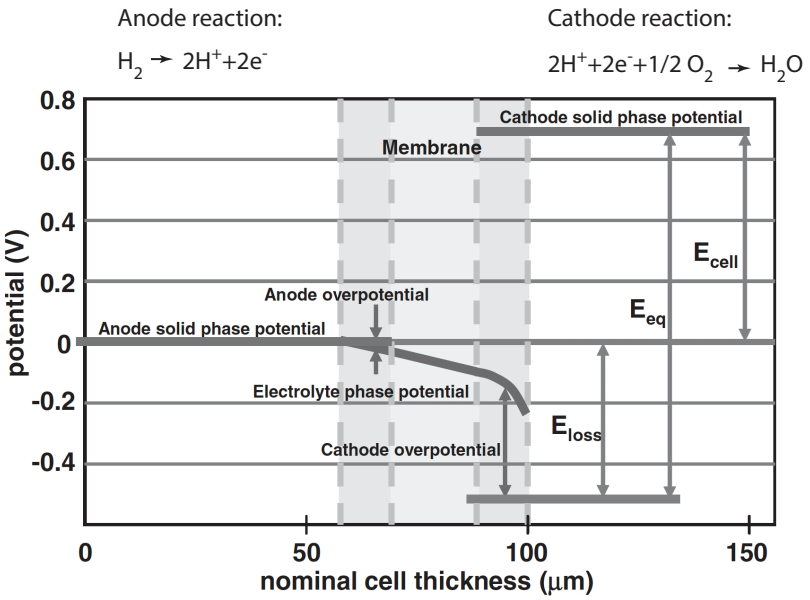

Figure 1.1: *Potential distribution in a hydrogen fuel cell cross-section showing voltage losses by location [2].*

2 Background

2.1 Nano-confinement

2.1.1 Structure and properties

Ionic liquids typically consist of ionic species with significant molecular asymmetry in at least one of the ions, which disfavours ordering of the ions into solid crystalline phases resulting in low melting temperatures and by narrower definition liquid state under 100 °C [14–16]. By suitable choice of the constituting anion and cation, ionic liquids can be designed to deliver various set of physical and chemical properties depending on the requirements for the envisioned application. Thus, the term "designer solvents" is often used for ionic liquids [11, 16].

However, it is important to consider that macroscopic properties can drastically change upon confinement of ionic liquids, depending on size, shape, and surface chemistry of the confining pore [7, 11]. As a first, simplified approach, one can assume that molecules that fill up a pore belong to two layers: a surface layer that is affected by the interactions with the pore wall and therefore showing different physical and chemical properties than in bulk, and an inner layer independent from the surface showing bulk-like properties, see Fig. 2.1 [11]. When the size of the confining pore is on the nanometer range, the molecules of the surface layer become more dominant in determining the properties of the confined IL due to their increased ratio. Experimental and computational studies have shown that in ionic liquids nano-confined in mesoporous materials phase transition temperatures, thermal stability, and molecular dynamics can both increase and decrease upon confinement depending on the chemistry of the pore wall [11].

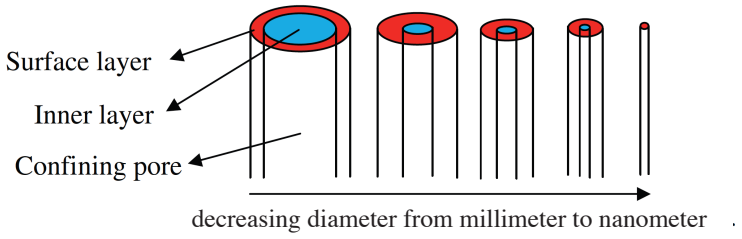

Figure 2.1: *Schematic of confined liquids in a cylindrical pore by decreasing pore-size to nanometer-scale [11].*

2.1.2 Proton transport in confined protic ionic liquids

Protic ionic liquids (PILs) are a unique group of ionic liquids that are distinct from conventionally known ionic liquids by possessing an exchangeable proton, most commonly on the cation [8, 9]. As an example for protic ionic liquids, the chemical structure of an alkyl-imidazolium protic ionic liquid is shown in Fig. 2.2. In addition to the vehicular type of charge transport that is typical of liquid electrolytes, PILs have the potential to contribute to the overall proton conduction *via* the Grotthuss mechanism (also called proton hopping) as well [8, 9, 12]. During the vehicular type of charge transport, the proton is chemically bound to the cation and therefore the ionic conductivity is limited by the diffusion rate of the cationic species [8]. However, when provided an appropriate hydrogen bonded network, protons can move *via* the Grotthuss mechanism much faster than the diffusing parent molecules, by means of a dynamic reorganisation of the involved hydrogen bonds [8, 9, 12]. In the case of alkyl-imidazolium based PILs, the imidazolium head of the cation can provide proton donor sites, while proton acceptor sites can be included by, for instance, the addition of an amphoteric molecule like imidazole [3, 9, 17]. In the context of developing electrochemical devices that operate by proton conduction, there is an obvious interest in materials in which the Grotthuss mechanism is thermodynamically favoured [8].

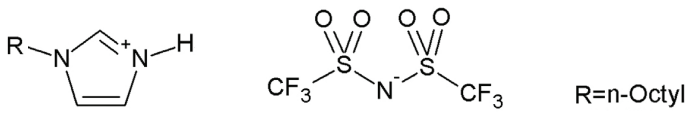

Figure 2.2: *Example of an alkyl-imidazolium protic ionic liquid: 1-octylimidazolium bis(trifluromethanesulfonyl)imide.*

Proton transport mechanisms and correlated local structures of PILs in nano-confinement fundamentally determine their proton conduction properties [3, 5, 6]. Nano-confinement of a PIL can impact the diffusivity of its constituting ions (both anions and cations) as well as the nature of the established hydrogen bonds, resulting in changed proton conduction properties compared to its bulk liquid state [3, 5]. In organic-inorganic hybrid materials made of imidazolium ionic liquids and mesoporous silicas diffusivity and network of hydrogen bonds have been primarily studied for the case of aprotic ionic liquids and only fewer contributions focused on the protic analogues [3, 5–7, 11, 18–21]. Aprotic and protic ionic liquids based on the alkyl-imidazolium cation have in common that both show nano-segregation into polar and non-polar domains even in their liquid phase, provided an alkyl chain on the cation longer than butyl, which increases the amphiphilic nature of the cation [22, 23]. Likewise, when they are nano-confined in mesoporous silica, both aprotic [18, 19] and protic [3, 5] alkyl-imidazolium ionic liquids show that their local structure on the nano-scale is strongly influenced by the chemistry of

the pore walls. When the silica walls are chemically untreated, and silanol groups (-SiOH) and non-bridging oxygens (-SiO^-) cover their surface, the polar domains of the ionic liquid orient towards the pore walls due to anion-silica and cation-silica interactions, leading to a dramatic decrease of the diffusivity of mainly the imidazolium cation (measurable by PFG-NMR) and of the macroscopically observed ionic conductivity (typically measured by impedance spectroscopy) [3, 5, 18, 19]. By contrast, hydrophobization of the silica walls, for example by functionalization of the wall with trioctylsilyl group when the confined ionic liquid had the same alkyl-chain length, namely HC_8ImTFSI, leads to the flipped-ion effect, by which the non-polar domains of the cation (i.e. the octyl chains) assemble at the pore wall. This is schematically shown in Fig. 2.3. Thus, there are only weak dispersion forces between the alkyl chains of the imidazolium cations and the hydrophobic groups covalently attached onto the silica walls allowing unrestricted, high diffusivities [3, 5, 18, 19]. Garaga et al. have recently reported that the HC_8ImTFSI/imidazole mixture confined in hydrophobized mesoporous silica displays a higher cation diffusivity than in the bulk pure ionic liquid, moreover, a decoupled proton motion was also observed with PFG-NMR [3].

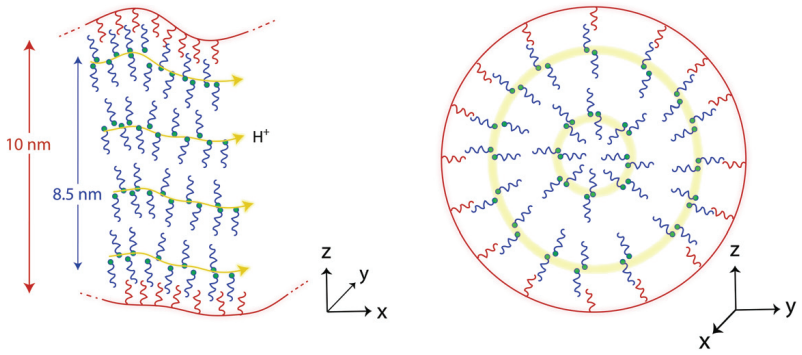

Figure 2.3: *Schematic picture of nanostructuration of [HC_8Im][TFSI]/imidazole mixture inside the nanopores of trioctylsilyl-functionalized silica showing the molecular organisation along the pores (left) and across a pore section (right) [3].*

2.2 Nano-scale templating

2.2.1 Sol-gel synthesis of silica matrix

Templating of silica with soft-templates is commonly carried out during sol-gel synthesis of the silica matrix, a term generally used for the synthesis of amorphous silica network from hydrolytic polycondensation of tetraalkoxy silane precursors even if gel formation does not necessarily occur [24]. One of the several advantages of the sol-gel method is the availability to use both chemical techniques and physical parameters to control the reaction sequence and in this way tune the properties of the product [24, 25]. The basic steps of the synthesis using tetraalkoxy silanes is (i) hydrolysis of the precursor that leads to formation of silanol groups, and (ii) condensation of silanol group contained monomers (with sufficiently high functionality) that leads to siloxane (Si-O-Si) linking groups and formation of silica network. Mechanisms and kinetics of hydrolysis in aqueous media are fundamentally determined by the pH; in case of tetraalkoxy silanes both acid and base catalyzed reactions proceed through S_N2 mechanism, Fig. 2.4.

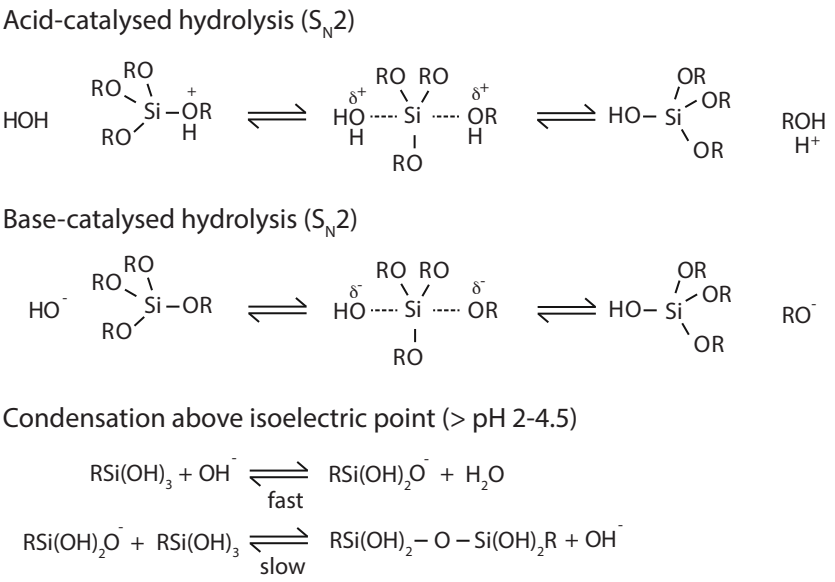

Figure 2.4: *Hydrolysis and condensation reactions during silica synthesis from tetraalkoxy silanes [25].*

The acid-catalyzed hydrolysis starts with the protonation of alkoxyde group that makes its electron withdrawing character enhanced resulting in the silicon atom being more electrophilic and susceptible to nucleophile attack. On the next step, water -acting as a nucleophile - attacks the silicium center forming bimolecular intermedier. The transition state consumed by displacement of alcohol accompanied by inversion of the silicon tetrahedron. Similarly *via* S_N2 mechanism, but with different nucleophile attack and intermedier, processes during base-catalysed

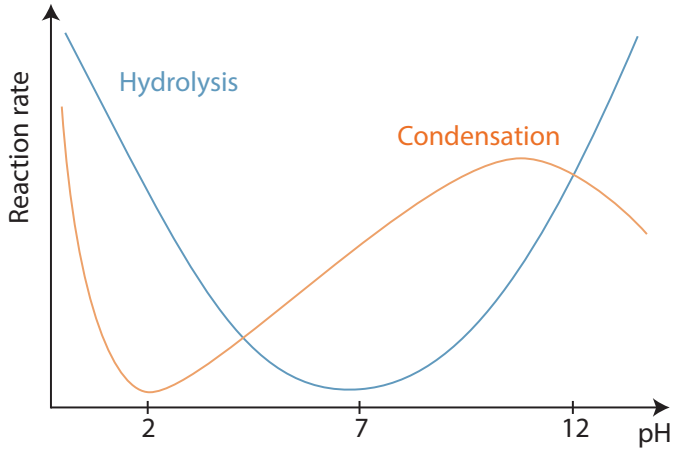

Figure 2.5: *pH dependence of reaction rate of hydrolysis and condensation reactions during silica synthesis from tetraalkoxy silanes [26].*

hydrolysis, thus the inversion of silicon tetrahedron occurs in this reaction pathway as well. As both acid and base can catalyse the hydrolysis, reaction rates are high in both pH extremes, Fig. 2.5 [25].

Condensation reaction of the hydrolysed silica precursor is also dependent on the pH, Fig. 2.5 and Fig. 2.6. Above the isoelectric point of silica (>pH 2-4.5), the deprotonated silanol can act as a nucleophile attacking on a neutral silicate specie. The acidity of the silanol (tendency to deprotonation) basically depends on the electron density on the Si center. When OR and OH ligands are replaced with siloxane bonded groups, the reduced electron density on Si increases the acidity of the protons on the remaining silanol groups. Therefore, reaction between larger, more highly condensed species with more acidic silanol groups and smaller, less weakly branched species is preferred. The condensation rate is maximized on basic pH and a minimum rate is observed near the isoelectric point. It is generally believed that the base-catalyzed condensation mechanism involves penta- or hexacoordinated silicon intermediates or transition states. On Fig. 2.6 the pH-dependency of silica products growths is schematically shown; on acidic pH and pH=7-10 in presence of salts three-dimensional network of amorphous silica, while in basic solution nanoparticle growth is observed.

2.2.2 Ionic liquids as templates

The soft-templating function of certain ionic liquids during synthesis of mesoporous silicas originates from their unique molecular structure. As mentioned previously, ionic liquids consist of ionic species with significant molecular asymmetry in at least one of the ions [14–16]. While ordering of ionic liquids into solid crystalline phase is disfavoured, nano-structuration still can occur in pure ionic liquids, in their mixtures with other molecular solvents, or in solvated form [22,

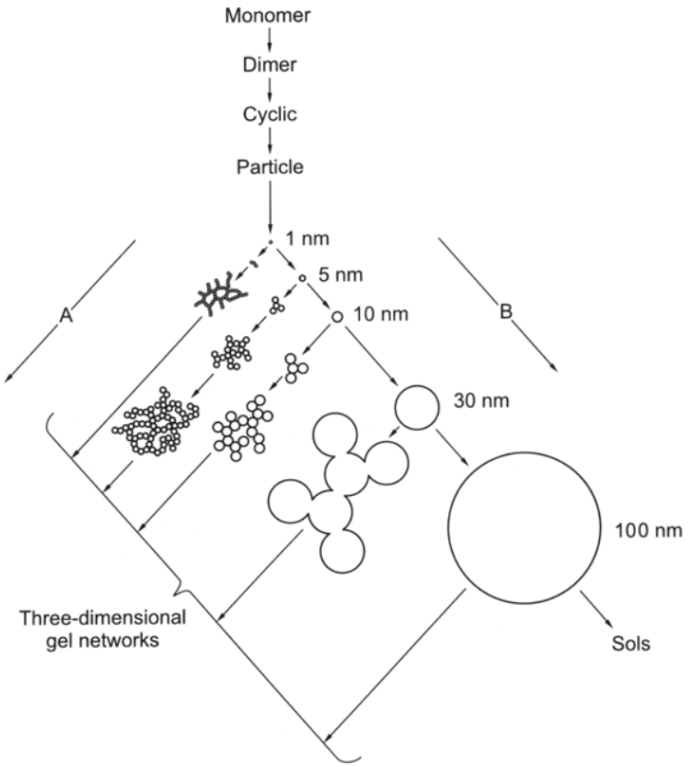

Figure 2.6: *Silica growth depending on pH. Pathway A: pH<7 or pH=7-10 with presence of salts. Pathway B: pH=7-10 in abscence of salt [25].*

27].

Structuration in ionic liquids takes place at different extent regarding the length scale, shape and kinetics with very wide variety among ionic liquids determined by their specific molecular structure [22, 27]. For example, in bulk, short chain alkyl imidazolium ionic liquids rather form more rapidly changing, disordered polar and non-polar domains [28], while in their long-chain counterparts, the longer alkyl chain enhances the amphiphilic nature of the cation to the point that the behaviour of the ionic liquid approaches that of surfactants leading to the possible formation of liquid crystalline phases [29]. Therefore, a subgroup of ionic liquids with strong amphiphilic nature is distinguished and referred to as surface active ionic liquids (SAILs) [30]. Among the alkyl-imidazolium ionic liquids with the chloride anion, $[C_6MIM]^+[Cl]^-$ is considered the "transitional ionic liquid", since it shows surface activity but no self-assembly in water [30].

Even though nano-structuration occurs, using ionic liquids as templates in the synthesis of mesoporous silica is not straightforward, and experiments have shown that the intrinsic structuration of the ionic liquids is not always efficient for the formation of mesopores in the silica network. Moreover, a cooperative interaction between the template and the silica-network forming species is often essential in

achieving a desired mesoporosity [31, 32]. For example, despite of the present supramolecular (e.g. ion cluster) and mesoscopic range (e.g. micro-phase separation, H-bond network) structurations in short-chain imidazolium ionic liquids, using them as the co-solvent during the sol-gel synthesis of silica usually leads to the formation of ionogels based on non-porous silica particles [22, 29, 33]. However, there is a very unique exception among short-chain imidazolium ionic liquids: $[C_4MIM]^+[BF_4]^-$, which has successfully been used as soft-template in the sol-gel synthesis of mesoporous silica under water-poor, acidic conditions by Zhou et. al. [32] The templating effect was explained by the authors with the so-called hydrogen bond-co-π-π stack mechanism, which involves hydrogen bonds formed between the $[BF_4]^-$ anions and the silanol groups of silica and the π-π stack interactions of the neighbouring imidazolium rings of the cations. The $[C_4MIM]^+[BF_4]^-$ formed worm-like pores in the obtained mesoporous monolith in which the $[BF_4]^-$ anions are assumed to be located along the pore walls while the imidazolium rings of the cations arrange next to the anions due to electrostatic attractions and are stacked parallel to each other due to π-π interactions, while their hydrophobic alkyl chains assemble towards the centre of the pores.

Compared to short-chain imidazolium ionic liquids, there are more, yet still limited in number, examples of syntheses with long-chain imidazolium ionic liquids being used as soft-templates to obtain mesoporous silica. Having water as solvent, amphiphilic ionic liquids that show amphiphilic self-assembly in aqueous medium, are more suitable soft-templates for the formation of different mesoporous silica structures *via* the sol-gel process [34]. Templating with $[C_nMIM]^+[Br]^-$ ionic liquids, where n is the number of carbon atoms in the straight alkyl chain attached to the imidazolium head, showed chain-length dependence in forming worm-like (n=8-12) and hexagonal (n=14-16) mesoporous silica [35]. With $[C_{16}MIM]^+[Cl]^-$ as soft-template, MCM-type hexagonal (MCM-41, with p6mm symmetry) and cubic gyroid (MCM-48, with Ia3d symmetry) silica could be obtained by tuning the concentration of the ionic liquid in the aqueous reaction solution [34]. Also, $[C_nMIM]^+[Cl]^-$ ionic liquids were able to form a lamellar pore structure in monolithic mesoporous silica, with the pore diameter being determined by the varying alkyl chain length and ranging from 1.2 nm (n=14) to 1.5 nm (n=18) [36, 37].

Despite of that more and more empirical information is gained on the templating behaviour of long-chain imidazolium ionic liquids in the sol-gel synthesis of mesoporous silicas, the underlying mechanism is often not studied nor even discussed. Fortunately, $[C_{16}MIM]^+[Cl]^-$ has many similarities with CTAB (cetyltrimethylammonium bromide), which comes handy in experimental design and basic understanding. However, there are also differences that become relevant in specific synthesis conditions of a desired pore structure [31]. As previously mentioned, cooperative interactions between the template and the silica-network forming species are crucial for pore formation on the nanometer scale. In the case of CTAB-templating at basic pH this cooperative interaction is dominantly

the electrostatic attraction between the cation of the surfactant [CTA^+] and the framework-forming negatively charged silicate oligomers [34]. It can be proposed that similar electrostatic attraction occurs between $[C_{16}MIM]^+$ and the silicate oligomers under the same reaction conditions [34]. However, it is important to note that being different in its chemical structure, the imidazolium head as an aromatic hereocycle is capable of establishing further interactions; as illustrated on a schematic of $[C_nMIM]^+$ in Fig. 2.7 [29]. Besides electrosctatic attraction, the presence of hydrogen bonds between the head groups and the silica precursor was proposed by Kaper et al., in agreement with a study by Wang et al. [31]. Further characteristic of the imidazolium head is the ability to arrange parallel due to π-π interactions between the aromatic rings, resulting in a higher packing density and a higher tendency to form mesostructures with lower curvature [31, 34]. Although present, the contribution of these additional interactions is weak, whereby CTAB (in which the binding affinity of the bromide ion is high) and $[C_{16}MIM]^+[Cl]^-$ in fact show very similar critical micellar concentrations (c.m.c.) and enthalpies of micellization [31].

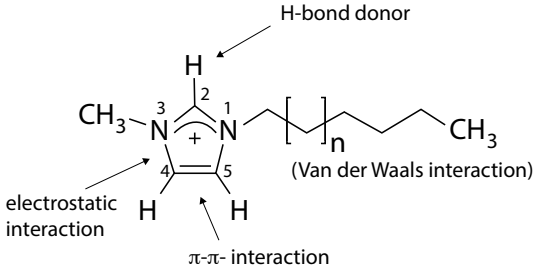

Figure 2.7: *Schematic of the possible interactions that the 1-alkyl-3-methyl-imidazolium cation is able to establish [29].*

2.2.3 Electrochemically assisted self-assembly (EASA)

For the preparation of soft-templated mesoporous thin films typically two robust techniques are used: evaporation-induced self-assembly (EISA) and electrochemically assisted self-assembly (EASA) that both are based on sol-gel synthesis [38]. Huge advantage of EASA is that vertical aligment of mesochannels can be achieved in extremely rapid synthesis (in a time scale of seconds seconds), however the conductivity of the substrate is a limiting requirement.

The schematic figure of mesoporous silica film preparation with EASA is shown on Fig. 2.8. First, an aqueous solution is prepared (in which ethanol:water=1:1 mixture is the solvent) with added precursor (TEOS) and template. After setting acidic pH, the precursor is let to be hydrolysed *via* acid catalysis [39]. Then, a three-electrode system is submerged into the solution. This contains a reference electrode, counter electrode, and a working electrode. The deposition of the silica film processes upon added potential; electrochemically-induced pH increase

created at the cathodic working electrode-solution interface, intended to produce hydroxyl ions that catalyzes rapid condensation of the silica onto the electrode surface. As the pH increases locally, acceleration of the polycondensation happens only close to the electrode surface [38]. Combined with the presence of the soft template, this method can be utilized in synthesis of mesostructured silica thin film with pore channels oriented perpendicular to the electrode surface [38]. Not only the formation of hydroxyl ions, but also orientation of the cationic surfactant on the electrode was proposed by Herzog et. al. [39].

In addition, the working electrode can be chosen according to the application. In literature, various materials were reported with different morphologies as working electrodes, e.g. ITO surface, and other conducting supports like macro discs or non-flat supports like gold CD-trodes and microelectrodes, including carbon fibers, platinum wires, and platinum microdiscs [39, 40]. Next to preparation of mesochannels in hexagonal arrangements, other mesostructural orders, e.g. three-dimensional cubic arrangement could be observed as well [38].

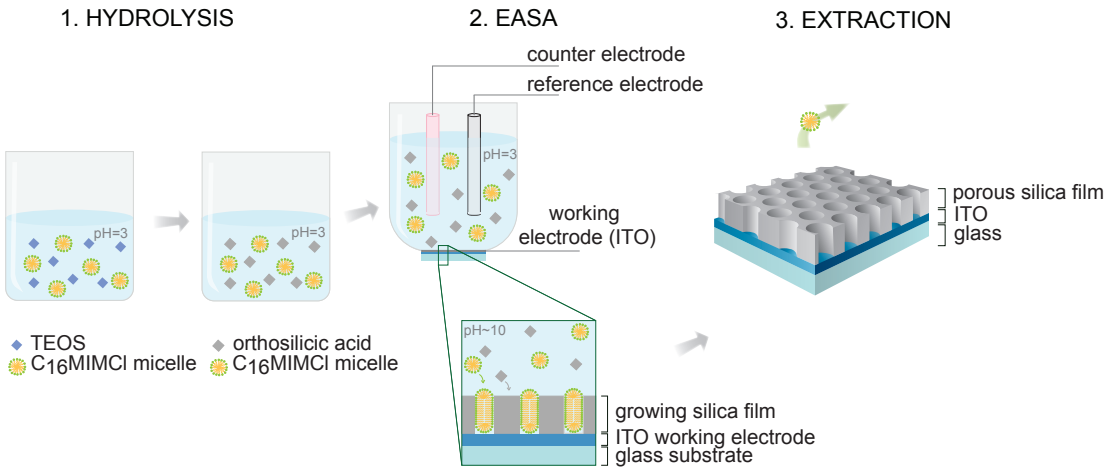

Figure 2.8: *Schematic illustration of the subsequent steps involved in EASA synthesis represented on IL-templated mesoporous silica thin films.*

3 Characterization and methods

3.1 Electron microscopy

3.1.1 Scanning electron microscope (SEM)

In a scanning electron microscope (SEM) a focused beam of high-energy electrons is used to generate a variety of signals at the surface of a sample specimen. For imaging, the acceleration voltage of the electron beam is typically set up to $\sim$ 15 kV and to obtain the scanning electron micrograph (i.e. image) most often secondary electrons are collected that are emitted from the sample as a result of interaction of the primary electron beam with the sample. As the energy of secondary electrons is relatively small (several 10 eV) only those generated from the upper surface of a few nanometers are able to escape from the sample and be collected. Therefore, use of secondary electrons for imaging is ideal for examining topography. In case of insulating samples, like silica, sputter coating with a good conductor is necessary to avoid charging effect (accumulation of electrons on the sample surface).

In this thesis SEM images were obtained with a JEOL 7800F Prime microscope in secondary electron imaging mode. Before imaging, the samples were coated with palladium for which an EMITECH K550x sputter coater was used. Cross sectional images of thin films were prepared by breaking the substrate after sputtering and imaging the broken surface on a tilted SEM stage.

3.1.2 Transmission electron microscope (TEM)

In a transmission electron microscope (TEM) the incident beam of electrons is accelerated to an energy of typically 80-300 keV. An array of magnetic lenses focuses the incident electrons into a small probe that is transmitted through the sample and then an image of the specimen is generated from the transmitted electrons. TEM is an excellent tool for imaging nanostructures as the theoretical resolution limit is extremely low due to the small de Broglie wavelength of the incident electrons that is on the range of 10^{-2} Å. In practice, the resolution of TEM instrument is much lower, but due to rapid instrumental improvement by date subnanometer resolution can be achieved. As an important requirement from the sample is that as a rule of thumb sample thickness has to be less than 100 nm. In case of thin films, a cross-sectional sample with the thickness of tens of

nanometers can be prepared with lift-out technique using FIB/SEM (focused ion-beam coupled SEM). Basically, a cross-sectional cut out of the film is prepared with ion-beam milling then the cut out is attached to a copper TEM grid. The attachment is formed with platinum deposition.

In this thesis, for top view TEM imaging of thin films, the samples were prepared by placing a droplet of sludge prepared from extracted, grinded films on a carbon-coated Cu TEM grid. Afterward, the samples were dried overnight under ambient conditions. The TEM experiments were carried out on a FEI Tecnai T20 instrument operating at 200 kV, and the obtained images were processed with the Digital Micrograph software to determine pore widths. For the cross-sectional TEM study, a sample of a thin film was prepared with the lift-out technique using a FIB/SEM (FEI Versa Dual FIB/SEM).

3.2 Small-angle X-ray scattering (SAXS)

Small-angle X-ray scattering (SAXS) technique is suitable to characterize structural features with typical dimensions from a few nanometers. SAXS is based on the scattering X-ray signal generated by differences in the average electron density on scales significantly larger than that of atomic radii [41]. Typical SAXS measurement with so-called transmission geometry is schematically shown on Fig. 3.1A. The intensity of the scattered X-ray in a point is defined by the wave vector (Q):

$$I(Q) = NV^2(\Delta\rho)^2 \left[F(Q)S(Q)\right]^2 + B \tag{3.1}$$

where N is number of scattering objects with volume V, $\Delta\rho$ is the electron-density contrast, F(q) is the form factor, S(q) is the structure factor, and B is a background signal. In our studies, we were able to gain information on the sizes of scattering objects from their diffraction peaks extracted from scattering patterns. So, based on Bragg‘s law, size was calculated from the structural correlation length, d, where q_{max} is the position of the diffraction peak:

$$d = 2\pi/q_{max} \tag{3.2}$$

In GISAXS (grazing-incidence small-angle X-ray scattering) mode the X-ray beam impinges on the sample surface under a shallow incident angle, typically of tenths of a degree. Then the X-ray photons scattered by the sample are collected with a two-dimensional detector, Fig. 3.1B. The interpretation of X-ray patterns were very similar to the X-ray scattering patterns produced in transmission geometry setup; in our studies hexagonal structure gave the same characteristic peak positions in GISAXS mode as described in literature for hexagonal pore structures in bulk measured in transmission geometry.

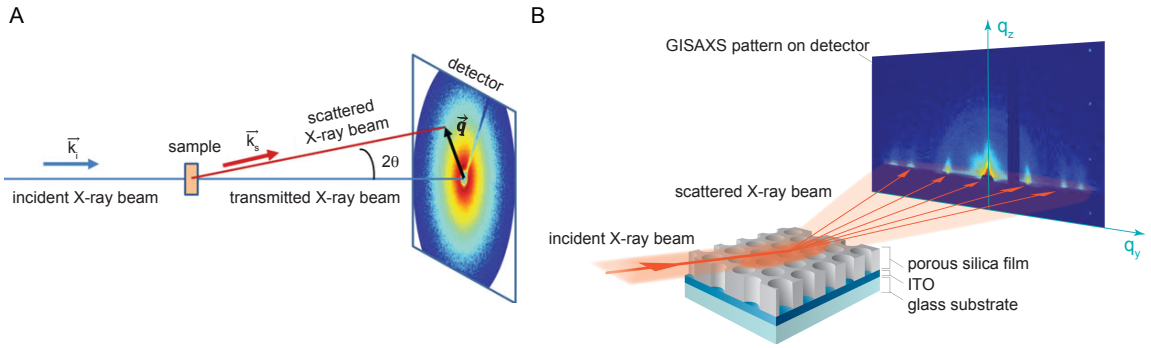

Figure 3.1: *SAXS. A: Schematic of SAXS experiment with so-called transmission geometry B: Schematic of GISAXS experiment [42].*

Small-angle X-ray scattering (SAXS) measurements were performed on a Mat:Nordic instrument from SAXSLAB/Xenocs. The X-ray beam was produced by a Cu-radiation source and focused with a Micro-Max 003 X-ray generator from Rigaku. Pilatus 300K from Dectris was used as the detector. X-ray scattering pattern of samples containing bulk ionic liquids and mesoporous silica particles were measured in a quartz capillary with inner diameter of 0.15 mm using transmission geometry setup of the instrument. The calibration was done with silver behenate. The sample to detector distance was set to 134 mm and the exposure time to 480 s. The collected 2D scattering patterns were further processed with SAXSGUI (Rigaku) software to transform them into 1D scattering graphs. The study of thin films was performed in grazing incidence mode of the instrument; by placing the samples on a GISAXS holder and aligning before each measurement. The sample to detector distance was 305 mm, the incidence angle 0.2°, and the exposure time 20 h. Scattering patterns were collected before and after measurement for 20 min to make sure that no radiation damage occurred. The collected 2D scattering patterns were further processed with the SAXSGUI (Rigaku) software by horizontal integration of intensities between q_z=0.01 $Å^{-1}$ and q_z=0.06 $Å^{-1}$, and subsequent plotting as a function of q_y.

3.3 Nitrogen adsorption

During the nitrogen adsorption measurement an adsorption isotherm (at T=77 K) is recorded that is in practice plotted as volume of nitrogen gas adsorbed on the sample versus the relative pressure (i.e. pressure/saturation vapor pressure). The adsorption isotherm is suitable to determine surface area, pore volume, and pore size distribution. Moreover, it provides information on enthalpy of nitrogen desorption and pore morphology of the studied porous material [43][44]. In case of mesoporous silicas, the surface area is commonly determined based on the BET (Brunauer-Emmett-Teller) method. For the use of this method several

assumptions are taken; (i) gas is considered ideal (ii) first a monolayer of nitrogen molecules forms during adsorption (iii) adsorbed molecules do not move on the surface (iv) enthapy of adsorption is equal on all sites of the sample surface while there is no adsorbate-adsorbate interaction and the enthalpy of adsorption for the second molecular layer equals to enthalpy of vaporization. The surface area is calculated from the volume of nitrogen monolayer adsorbed on the sample, V_m, by using the area occupied by an adsorbed molecule. V_m is determined from the fitting of BET equation on the linear range of the isotherm typically at p/p_0=0.05-0.3 and interpolated to the ordinate;

$$\frac{p}{V\left(p_0 - p\right)} = \frac{1}{V_m C} + \frac{C-1}{V_m C}\left(\frac{p}{p_0}\right) \tag{3.3}$$

where p (partial pressure of the nitrogen) and V (volume of nitrogen adsorbed) are known from the adsorption isotherm, p_0 (saturation vapor pressure) is well-defined parameter for a given temperature, while V_m and C-value are determined from the slope and intersection. The C-value is theoretically related to enthapy of desorption ($\Delta_{des}H$) and enthalpy of vaporization ($\Delta_{vap}H$);

$$C = e^{\frac{\Delta_{des}H - \Delta_{vap}H}{RT}} \tag{3.4}$$

Even though with assuming that desorption and adsorption enthalpies are equal ($\Delta_{des}H$=$\Delta_{ads}H$), thus $\Delta_{ads}H$ could be technically calculated, it is not accurate enough to do so and thus for exact measurement calorimetric methods are preferred. However, it is worth to keep in mind that a higher C-value indicates a higher difference between $\Delta_{des}H$ and $\Delta_{vap}H$ and the assumption of monolayer formation is more valid. In general, BET method is used if C > 2. The pore size distribution can be determined with the BJH (Barrett-Joyner-Halenda) method, typically using the adsorption isotherm. This method applies the modified Kelvin equation with the assumption of cylindrical pores. As a commonly used method its validity has been studied widely and confirmed for various mesoporous materials, however it has been also shown that for narrow mesopores the pore size is slightly underestimated. For gaining the total pore volume the Gurvich rule is applied, which assumes that when the pores are filled (p/p_0>0.95), the adsorbed ammount of nitrogen is in liquid state and therefore its volume in the pores is quantifiable.

In this thesis, nitrogen adsorption was measured on a TriStar 3000 instrument from Micromeritics after outgassing treatment of the sample for overnight at 120°C under a nitrogen flow. The surface area was determined using the BET (Brunauer-Emmett-Teller) method, the pore size distribution was calculated with BJH (Barrett-Joyner-Halenda) method, and the total pore volume was determined by applying the Gurvich rule at p/p_0=0.98.

3.4 X-ray photoelectron spectroscopy (XPS)

X-ray photoelectron spectroscopy (XPS) is a surface sensitive analytical technique suitable for qualitative and quantitative chemical analysis and electronic structure study of a material. The technique is based upon photoelectric effect; electrons (photoelectrons) are emitted from matter due to energy uptake through absorption of incoming X-ray radiation with sufficiently high frequency, see Fig. 3.2. The excited photoelectrons travel through the sample to the surface and escape into the vacuum. Then, the photoelectrons are collected and their kinetic energies are measured. From the measured kinetic energy of a photoelectron its binding energy can be calculated:

$$h\nu = E_B + E_K + \Phi \tag{3.5}$$

where hν is the energy of the incoming photon, E_B is the binding energy, E_K is the kinetic energy of the photoelectron, and Φ is work function term. The electron binding energy (ionization energy) is characteristic to the element from which the electron was emitted and therefore elemental compostiton of the surface can be determined. The huge advantage of XPS is that most, even lighter, elements can be detected with high sensitivity. Also a surface sensitive method; XPS spectra gives information on the topmost few nanometers of a solid sample as this is the typical escape depth of the photoelectrons.

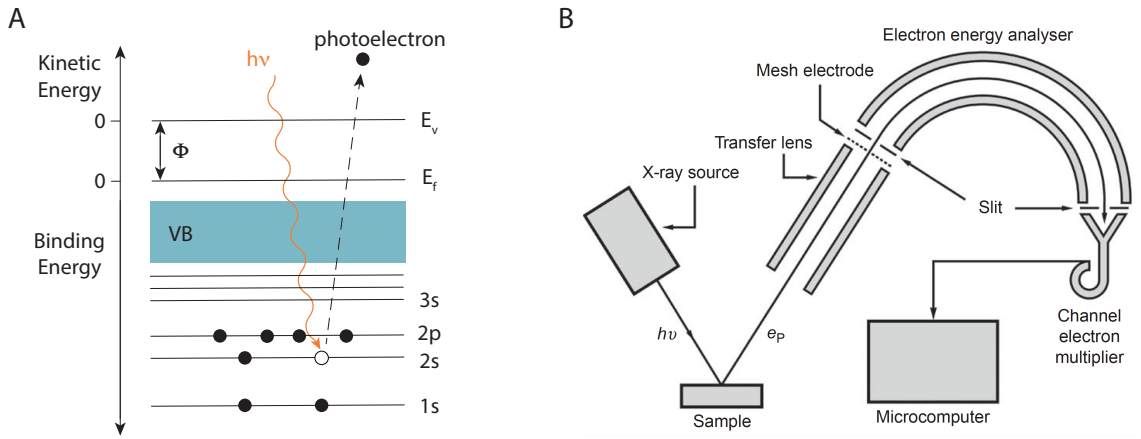

Figure 3.2: *XPS. A: Example of photoelectron emission from an oxygen atom shown on its energy level diagram B: Basic schematic of an X-ray photoelectron spectroscope setup [45].*

X-ray photoelectron spectroscopic measurements were carried out on Quantum 2000 scanning ESCA microprobe from Physical Electronics with AlKα (1.486 keV) beam at an incidence angle of 45° relative to the sample surface. The MultiPAK software package was used to determine the atomic concentration. Photoelectrons were collected on approximately 500 x 500 μm^2 large areas.

3.5 Vibrational spectroscopy

The energy of a molecule is quantized, thus allowed to have only certain discrete energy levels. This energy is the sum of contributions from its different modes of motion and electronic contribution:

$$\varepsilon_i = \varepsilon_i^T + \varepsilon_i^R + \varepsilon_i^V + \varepsilon_i^E \tag{3.6}$$

where T denotes translation, R rotation, V vibration, and E the electronic contribution. The order of magnitude of the excitation energy depends on the type of the inital and end energy level, Fig. 3.3[44]. In case of vibrational excitation this is around the energy of a 10^2-10^3 cm^{-1} wavelength electromagnetic wave. In vibrational spectroscopic methods vibrational excitation is induced with photon irradiation and allow the quantitative and qualitative study of vibrational motions that are characteristic to chemical groups and their chemical environment. The modes of vibrations, that are listed in Table 3.1, are often modelled with a harmonic oscillator that gives a good description for the v=0→1 transition, Fig. 3.4. The number of vibrational modes of a molecule can be determined from the number of atoms that it contains (N); a non linear molecule possesses 2N-6, linear possesses 3N-5. The vibrational energies usually follow the order: ν(stretching)> δ(in-plane bending)> γ(out-of-plane bending)> τ(torsion).

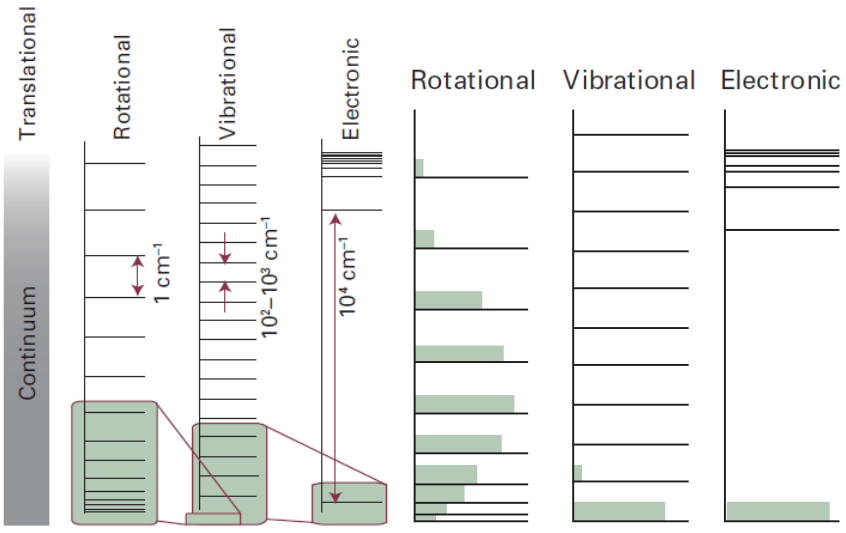

Figure 3.3: *Energy level separations expressed as wavenumbers (left) and Boltzmann distribution of populations for rotation, vibration, and electronic energy levels at room temperature [44].*

Table 3.1: *Vibrational Modes*

Symbol	Name	Mode of deformation
ν	stretch	stretching of valence bond
δ	in-plane bend	one or more bond angle changes, constant bond length
γ	out-of-plane bend	one atom oscillates through a plane of at least the atoms
τ	torsion	dihedral angle is changed

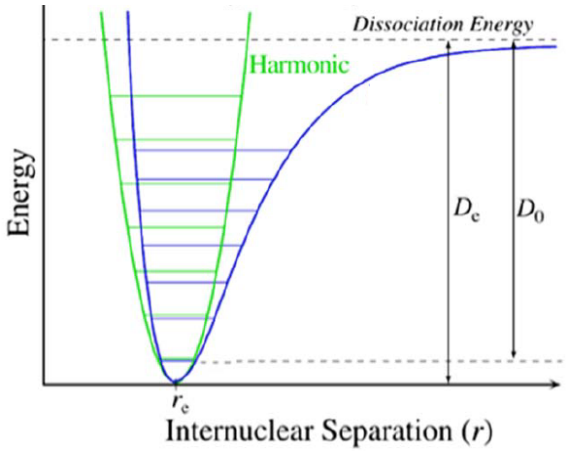

Figure 3.4: *The parabolic potential energy as a simple harmonic oscillator and the actual potential energy .*

3.5.1 Infrared spectroscopy (IR)

In infrared spectroscopy the necessary energy for vibrational excitation is supplied by absorption of infrared light. By convention, transmittance through the sample is plotted as a function of wavenumber of the incident infrared light. The infrared spectrum is typically taken on 4000-400 cm^{-1} wavenumber range that energy on room temperature induces v=0→1 transition in most vibration modes due to high population of the ground state (v=0). Though, weak so-called overtone bands might appear on the spectra from v=Δ2 transitions. Important to note, that when vibrational excitation is generated by absorption of electromagnetic wave the resonance condition requires that the frequency of the radiation equals that of the vibration and that the dipole moment of the atoms involved in the vibration changes. Thus, generally polar bonds display high intensity of infrared absorption. Also, peaks on infrared absorption spectra broaden due to the different rotational states of the vibrationally excited molecules (however it is not the only reason of peak broadening). To improve signal-to-noise ratio, infrared spectrometers contain interferometers that allow the use of high intensity polychromatic incident beam instead of scanning the wavenumber spectrum stepwise. Basically, the beam is splitted and one part of the beam is refracted towards a fixed mirror and the other is transmitted towards a moving mirror, then

they reflected from the two mirrors back to the beam splitter and directed to the sample. After passing the sample, the beam is collected on the detector. The difference in optical path length between the two parts of the splitted beam is known as the retardation or optical path difference (OPD) and the interferogram is obtained by varying the OPD and recording the signal from the detector for its various values. Then, the interferogram is converted to transmittance spectrum through Fourier-transformation. Therefore, the described method is called FT-IR (Fourier-transform infrared spetroscopy).

Attenuated total reflectance IR specroscopy (ATR-IR)

When the IR spectrum is obtained in ATR-mode, an ATR accessory is placed in the pathway of the IR beam. The most important part of it is the ATR crystal that has high refractive index and good infrared transmission. Therefore within the planar crystal several internal reflections occur, depending on the incident angle of the incoming beam. The sample to be investigated is placed in contact with the crystal. As it can be seen in Fig. 3.5, at the reflection points the incident light penetrates into the sample as an evenescent wave. The reflection will be attenuated if the frequency of the incident light is within the range of the absorption frequencies of the material while the IR photons with frequencies far from the absorption region will be totally reflected. The complex refractive index (ν) of the sample consist of a real part and an imaginary part:

$$\nu = n + ik \tag{3.7}$$

where n, the real part, is the refractive index when there is no absorption and the imaginary part relates to attenuation when absorption occurs. As κ is related to the extinction coefficient in the Lambert-Beer law, absorption spectrum can be measured from the collected IR beam. The penetration depth (d_p) is usually in the order of 2-15 μm.

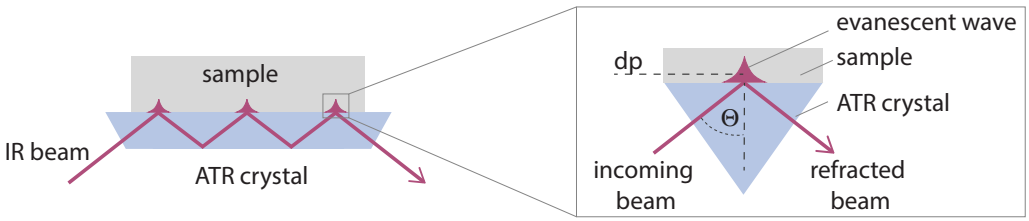

Figure 3.5: *Schematic of attenuated total reflectance used in ATR-IR instruments.*

The ATR-IR spectra were recorded on a PerkinElmer Fourier transform infrared (FT-IR) spectrophotometer in attenuated total reflectance (ATR) mode with a single reflection diamond ATR crystal (GladiATR, Pike Technologies). As diamond ATR crystal was used, the spectra were cut between 2600 and 1900 cm^{-1}. The full optical range was obtained from 4000 cm^{-1} to 400 cm^{-1} with 1

cm^{-1} resolution. For all experiments 64 scans were collected and averaged. The recorded data was subjected to baseline correction.

Transmission-reflection IR spectroscopy

Transmission-reflection spectroscopy is a spectral technique especially suitable for studying ultrathin films on a reflective, smooth substrate. During the measurement most of the incoming IR beam penetrates the surface of the film and is reflected at the substrate, see Fig. 3.6. In this way the light passes through the surface layer twice, leading to increased intensity of the absorption spectrum as compared to conventional transmission.

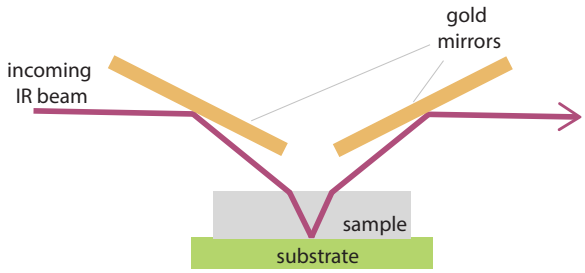

Figure 3.6: *Schematic of the transmission-reflection mode in the sample*

Vibrational spectra were recorded with a PerkinElmer Fourier transform infrared (FT-IR) spectrophotometer. The measured spectral range was from 4000 cm^{-1} to 400 cm^{-1} and the resolution was set to 4 cm^{-1}. For all experiments, 64 scans were collected and averaged. The recorded data were baseline corrected.

3.5.2 Raman spectroscopy

In Raman spectroscopy vibrational excitation in the studied material is induced through inelastic scattering of a monochromatic, high intensity, coherent light beam with suitable wavelength (UV to near-infrared laser). During the inelastic photon scattering (Raman scattering) the energy of the scattered photon changes according to the energy input or output related to the change in vibrational state of the material, Fig. 3.7. When the material is excited to a higher vibrational state the energy of the scattered light gets lowered with the energy difference of these states and the scattering is called Stokes scattering. In opposite case, when the material is already at higher vibrational state and gets to a lower one during the scattering process, the excess energy is taken up by the scattered photon and the process is called anti-Stokes scattering. Elastic scattering without energy change of the photon is the Rayleigh scattering and most of the incoming photons scatter in this way. Therefore, laser is used to gain high enough flux of elastically scattered photons. As at room temperature most of the molecules are in ground vibrational state, Stokes scattering has higher probability than anti-Stokes and

the energy shift (Raman shift) relative to the energy of the incoming photon is measured from the energy of the Stokes scattered photons.

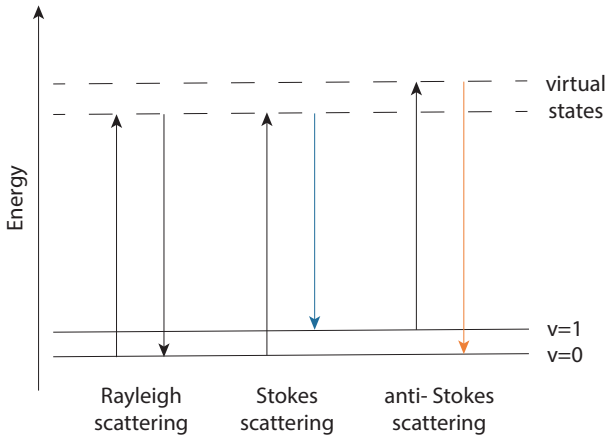

Figure 3.7: *Rayleigh, Stokes, and anti-Stokes scattering.*

The intensity of Raman scattering radiation is defined by the following relation:

$$I_R \propto \nu^4 I_0 N \left(\frac{\delta\alpha}{\delta Q}\right)^2 \tag{3.8}$$

where I_0 is the incident laser intensity, N is the number of scattering molecules, ν is the frequency of the exciting laser, α is the polarizability of the molecular bond, and Q is the vibrational amplitude. The polarizability of the molecule, α, determines Raman activity of the molecular vibration. As a general rule, vibrational modes that are Raman active are usually inactive in infrared spectroscopy and *vice versa*. Therefore Raman and infrared spectroscopies are typically used complementary.

Confocal Raman spectroscopy is an excellent method for chemical mapping in 2D and 3D with micrometer resolution; in our studies it has been used for mapping of ionic liquid-filled mesoporous silica microparticles. The schematic of the measurement steps is shown on Fig. 3.8 [3]. In brief, over a selected area of particles the confocal point is set at a half-diameter height of the particles and the most intense Raman peak of the ionic liquid was used as the probe signal to obtain spatial information on the location of the liquid phase. The shown 2D map is created by transforming the integrated intensity of the selected peak into a color code at every collection point (red for more intense and black for less intense).

For chemical characterization of nano-confined ionic liquids in mesoporous silica, Raman point spectra were obtained with a Renishaw InVia Reflex Raman spectrophotometer equipped with CCD detector and X100 LWD Leica objective. A 532 nm wavelength diode laser was used for vibrational excitation while the grating was 2400 grooves/mm, covering spectral range of 100-4000 cm^{-1}. The confocal Raman mapping was carried out with the same equipment, using 532

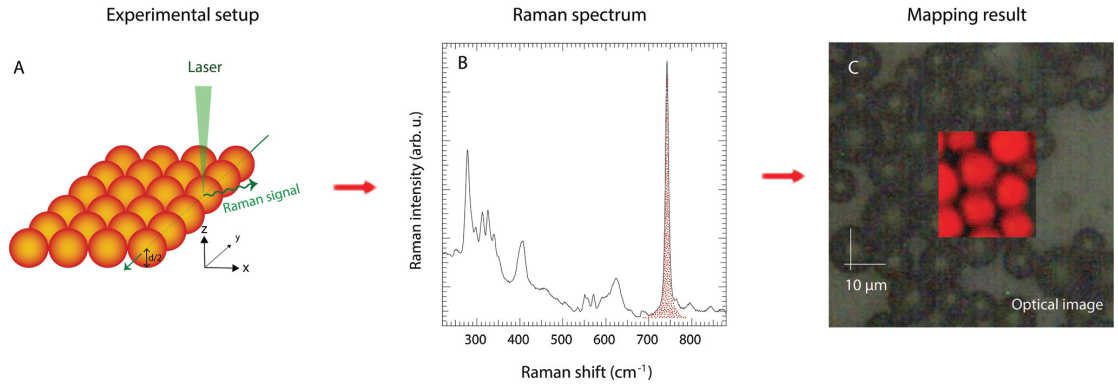

Figure 3.8: *Surface mapping experiments by confocal Raman spectroscopy performed over silica particles filled with ionic liquid [3].*

nm wavelength diode laser. Before each measurement the spectrophotometer was calibrated to the 1^{st} order band at 520.6 cm^{-1} of Si wafer.

3.6 Cyclic voltammetry (CV)

Cyclic voltammetry is a powerful tool to study electron transfer involved in an electrochemical reaction. Characterizing electron transfer provides information not only on the electrochemical change itself, but also other parameters that can influence it. Cyclic voltammetric measurement is carried out in a three electrode electrochemical cell, containing a reference electrode with well-defined and stable equilibrium potential, an inert counter electrode, and the working electrode, all immersed in an electrolyte solution, see Fig. 3.9A. When the aim is to study the working electrode, an electrochemical probe (or redox probe) is added to the electrolyte, which is a substance with known electrochemical behaviour. Typically, metal complexes are used for such purpose. The voltammogram is obtained by recording current as a function of sweeping voltage applied on the working electrode relative to the reference electrode. To ensure that the kinetics of the redox reaction at the counter electrode do not inhibit the reaction at the working electrode, the surface area of the counter electrode has to be greater than that of the working electrode. A typical voltammogram of a redox probe with oxidation number change of one is plotted on Fig. 3.9B. The equilibrium between the oxidized and the reduced form of the probe is described with the Nernst equation:

$$E = E^0 + \frac{RT}{F} ln \frac{(a_{ox})}{(a_{red})} \approx E^{0'} + \frac{RT}{F} ln \frac{[ox]}{[red]} \tag{3.9}$$

where E^0 is the standard potential, $E^{0'}$ is the formal potential and the relative activities (a) of the oxidized (ox) and reduced (red) forms of the probe in the system at equilibrium are approximated with their concentrations. Furthermore,

F is Faraday constant, R is the universal gas constant, and T is the temperature. When a solution of the oxidized form is scanned to negative potentials, it gets reduced locally at the electrode, resulting in concentration increase of the reduced form at the surface of the electrode and the mass transport of the oxidized form toward the electrode becomes limited. If the redox reaction is reversible, similar phenomena occurs in the reverse scan and therefore the voltammogram shows so-called duck-shape. Thus, the shape of the oxidation and reduction peaks provides information on the diffusion of the redox probe near the electrode.

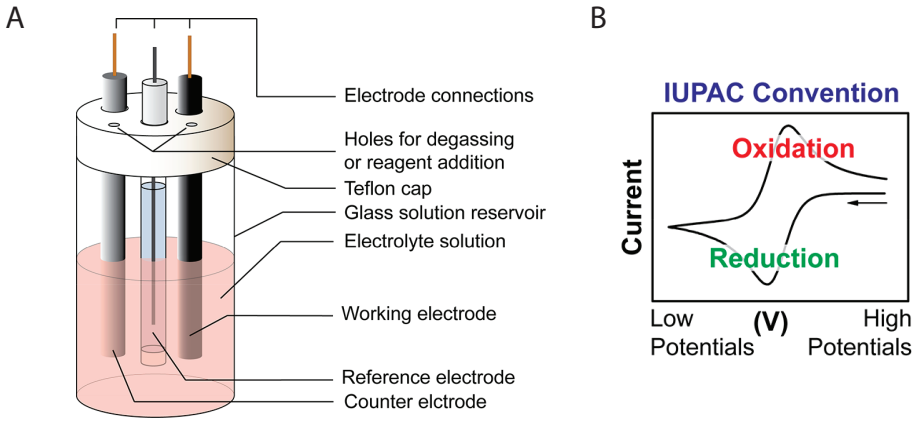

Figure 3.9: *Cyclic voltammetry. A: Electrochemical cell used for cyclic voltammetric measurement B: Voltammogram of a redox probe with oxidation number charge of one [46].*

In our studies cyclic voltammetry was used to characterize the permeability of IL-templated silica thin films to cations, here Ru(III). The measurements were carried out in a three-electrode system that contained a stainless steel counter electrode, a Ag/AgCl reference electrode (Metrohm), and a bare ITO plate or ITO plate with the deposited silica film on it as the working electrode. The aqueous electrolyte solution contained 0.5 mM $Ru(NH_3)_6{}^{3+}$ and 0.1 M $NaNO_3$, while the contact area with the solution was 0.5 cm^2. The voltammogram curves were recorded with a μAutolab III potentiostat (Eco Chemie) at a scan rate of 20 mV/s.

3.7 Impedance spectroscopy

Impedance spectroscopy is a commonly used technique to characterize electrical properties of devices or materials by the impedance function $Z^*(\omega)$. In practice, the sample is placed in-between two electrical ports (electrode plates) having known geometry defined by the distance and areas of the ports. Then, alternating voltage U_0 is applied to the sample with a fixed frequency $\omega/2\pi$ that induces current I_0 with the same frequency in the sample. The occurring phase shift

between the alternating current and the voltage can be described with phase angle, ϕ. The ratio of U_0 and I_0, and the phase angle, ϕ are determined by the electrical properties of the sample. For simple calculation and representation of the formulas, voltage and current are convenient to be used in complex notation, and from them the impedance function can be expressed:

$$U(t)^*(\omega) = U_0 cos(\omega t) \tag{3.10}$$

$$I(t)^*(\omega) = I_0 cos(\omega t + \phi) \tag{3.11}$$

$$Z(t)^*(\omega) = \frac{U^*(\omega)}{I^*(\omega)} \tag{3.12}$$

The impedance spectrum is obtained by taking measurement points with varying frequencies (ω) of the alternating voltage. Different frequency ranges of the impedance spectrum give information on different types of responses of a material to the applied alternating voltage as these responses have characteristic time constant associated with them. For example, studying ionic conduction of ionic liquid-based systems as a function of temperature of -40°C and 135°C, the suitable frequency range was 10^{-1} - 10^7 Hz.

The conductivity measurements were carried out on a broadband dielectric spectrometer (Novocontrol GmbH). The samples were placed between two gold-plated brass electrodes with a diameter of 13.5 mm. The thickness of each sample was 1 mm; using a silica spacer. Conductivity data were collected in 10 °C intervals and the stabilization time was set to 600 s at each temperature.

4 Results and discussion

This thesis is based on two studies of different IL/silica hybrid materials presented in Paper I and Paper II. In the first study (Paper I) the molecular dynamics and related local structure of an imidazole/PIL mixture confined in hydrophobized mesoporous silica particles has been investigated by characterization of a sample series with varying liquid-to-silica ratios. Furthermore, we used the same PIL/imidazole mixture as Garaga et al. [3], here, we investigate also the impact of downsizing the pores from 10 nm to only about 5 to 6 nm on transport properties and related structuration. In the second study (Paper II) it has been demonstrated that a long-chain imidazolium IL is suitable for formation of vertically-aligned nanochannels in silica thin films *via* EASA method. As the first reported use of an IL in EASA method, the verification of the synthesis procedure and the possible underlying templating mechanism will be discussed in-depth.

4.1 Transport properties of PIL/silica hybrid materials

4.1.1 Ionic conductivity and self-diffusion

Ionic conductivity of various PIL/silica hybrid materials with varying liquid-to-silica ratio was characterized with impedance spectroscopy, also reported in Paper I. The hybrid materials consisted in a liquid phase of imidazole/HC_8ImTFSI mixture ("Im/PIL mixture") and a solid phase of mesoporous silica microparticles hydrophobized with trioctylsilyl-groups ("5-C8-SiO_2"), the SEM image of neat 5-C8-SiO_2 and its differential pore size distribution is shown in Fig. 4.1. In addition, the liquid-to-silica ratio was expressed also as pore filling in unit of %, indicating how much of the available pore volume of the mesoporous silica was occupied by the added Im/PIL mixture. The measured ionic conductivites of the samples are shown in Fig. 4.2 A as a function of temperature on an Arrhenius plot. In all of the studied PIL/silica hybrid materials, conductivity has non-linear dependence on temperature, typical for ionic liquids and liquid electrolytes in which vehicular mechanism is the dominating charge transport mechanism. Accordingly, VFT (Vogel-Fulcher-Tamman) equation, $\sigma_{VFT} = \sigma_\infty \cdot e^{-(DT0)/(T-T0)}$, wasused to fit the experimental data points [47], the determined variables are summarized in Table 4.1.

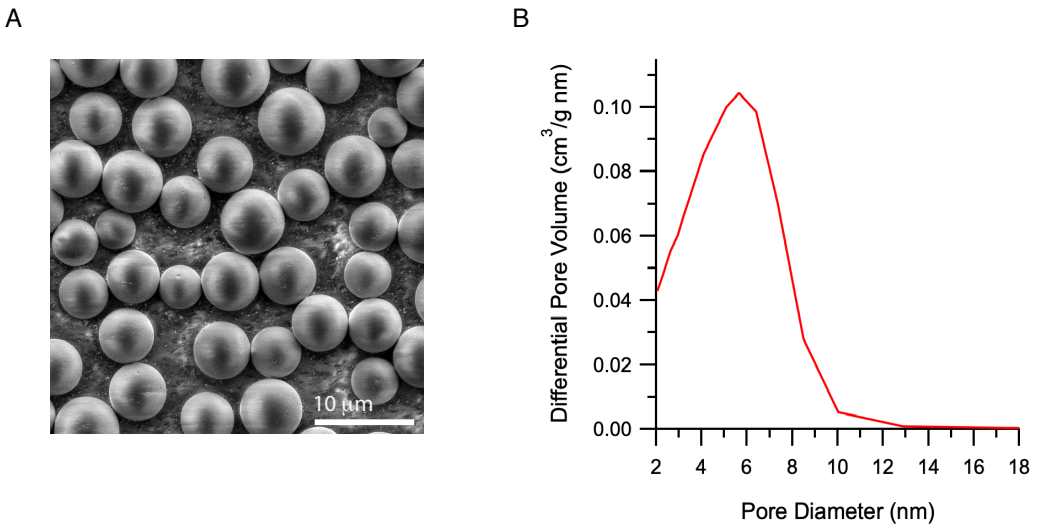

Figure 4.1: *A: Scanning electron microscopic (SEM) image of the pristine 5-C8-SiO_2 mesoporous silica microparticles. B: Differential pore size distribution obtained for the 5-C8-SiO_2 neat microparticles, determined with nitrogen adsorption.*

Table 4.1: *Values of D, T_0, andσ_∞, as found from fitting the conductivity data with the empirical VFT equation $\sigma_{VFT} = \sigma_\infty \cdot e^{-(DT0)/(T-T0)}$.*

Pore filling	Material Type	σ_∞ (Scm^{-1})	D (–)	T_0 (K)
0%	dry powder	–	–	–
50%	wet powder	0.0002	4.5	175
100%	wet powder	0.03	4.7	155
200%	suspension	0.10	4.3	157
400%	suspension	0.13	4.6	155
Im/PIL	liquid	0.20	4.0	157

In the VFT equation, D is a parameter related to fragility, T_0 is a temperature related to, and typically lower than, the glass transition temperature T_g, and σ_∞ is the conductivity extrapolated for infinite temperatures. While D does not change significantly with composition and value of T_0 is also very little dependent on the degree of pore filling σ_∞ clearly decreases with decreasing relative amount of the liquid phase, which was observed for any temperature. The lower conductivity upon increased volume fraction of silica is better illustrated in Figure 4.2 B, for the arbitrarily selected temperatures of 15 °C and 95 °C. This rapid decrease is significant even after compensation for the molar concentrations and may be attributed to changed or lost connectivity between the ionic species occuring on different extent depending on the type of the given material, since the solid phase

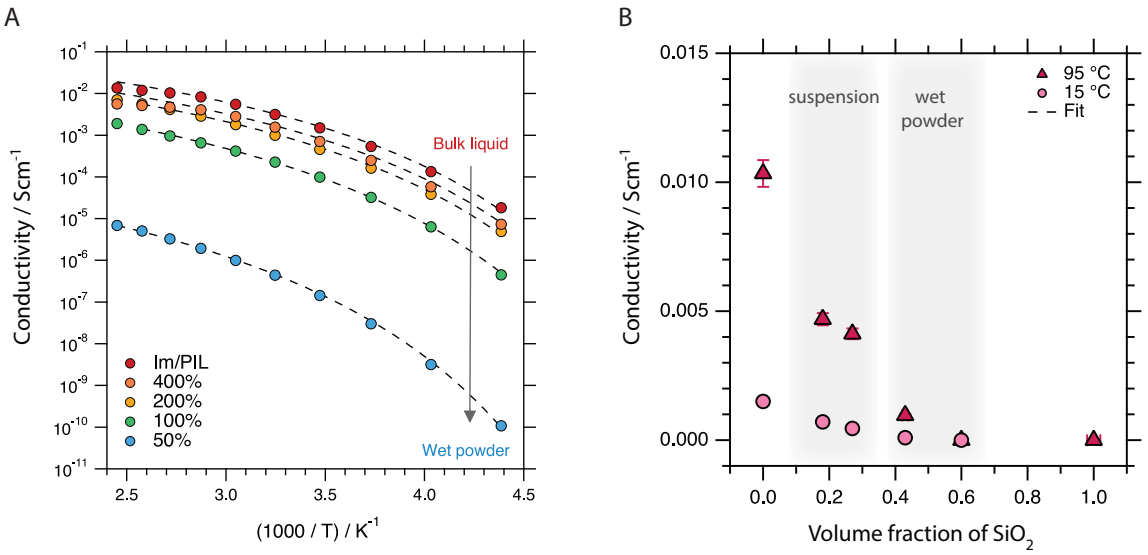

Figure 4.2: *A: Arrhenius plot of conductivity values measured for the different samples investigated and covering the temperature range –50 – 145 °C. Dashed lines are simple guides to the eye. B: Absolute values of conductivity measured at 15 and 95° C as a function of the volume fraction of silica.*

of porous silica creates longer and likely tortuous ion diffusion pathways as well as discontinuities in the longer spatial range.

Table 4.2: *Self-diffusion coefficients (in units of 10^{-11} m^2/s) measured for the different samples using selected ^1H resonances. [a] Data retrieved from a previous work, see reference [3]. * Estimated values based on certain assumptions (see text).*

Pore filling	D_{cat}	D_{NH}	D_{Im}	D_H	D_H/D_{cat}
0%	–	–	–	–	–
50%	0.95	n.a.	n.a.	–	–
100%	0.87	n.a.	n.a.	–	–
200%	1.63	2.31	2.25*	5.5	3.4
400%	1.66	2.60	2.36*	7.2	4.3
Im/PIL[a]	0.86	1.35	1.24	3.7	4.3

The transport properties of the Im/PIL mixture while confined in the mesopores of 5-C8-SiO_2 microparticles were also monitored by diffusion NMR measurements,

the self-diffusion coefficients are summarized in Table 4.2. For all samples, the self-diffusion coefficients of the imidazolium cation were determined directly from the ^{1}H resonance of its CH_2 and CH_3 groups in the octyl chain. Due to peak broadening upon decreased liquid-to-silica ratio, the self-diffusion coefficients of the -NH group (to which both -NH groups of imidazole and imidazolium contribute) could be determined only in samples with pore fillings of 200% and 400%. In addition, the D_{Im} values were estimated assuming the same D_{NH}/D_{Im} and D_{Im}/D_{cat} ratios in the mesopores as for the case of the neat Im/PIL mixture, desicribed more detailed in Paper I and in reference [3].

The diffusion NMR results indicate that the imidazolium cation, and under our assumptions also imidazole, not only move faster as the pore filling increases, but also the nano-confinement has no adverse effect on their diffusivity when it takes place in hydrophobized silica mesopores. More precisely, the samples with 50% and the 100% pore fillings, and the samples with 200% and 400% pore fillings, show pair wise similar behaviours. The proton sitting on the -NH group, displays self-diffusion values systematically higher than that of the imidazolium cation itself, suggesting a transport mechanism that is not exclusively vehicular. Moreover, if we consider estimated values, the exchangeable protons on the -NH group diffuse, on average, faster than their parent molecules, in the hybrid materials investigated here about 3 to 4 times faster than the imidazolium cation. This is very similar to the case described by Garaga et al. for the 10 nm large pores [3], and supports the idea presented in this previous work that the coexistence with mesoporous microparticles can result in enhanced dynamical effects in PILs. It appears also that the liquid phases outside and inside the mesopores have distinct dynamical properties, with a D_{cat} clearly higher outside. At this stage we don't have a conclusive explanation for this difference, one can assume that it is related to locally different molecular ordering and/or different ionic densities inside and outside of the microparticles.

4.1.2 Structure and interactions

With the purpose of getting insight into the local structure within the pores, X-ray scattering experiments were performed on the PIL/silica hybrid materials at room temperature. The changes in X-ray scattering pattern upon composition is shown in Figure 4.3 A. The bulk Im/PIL liquid, i.e. the HC_8ImTFSI/imidazole mixture, shows three characteristic peaks which have already been discussed for numerous protic and aprotic ionic liquids [23, 48–50]. Accordingly, the peak centered at 0.84 $Å^{-1}$ arises from all ion-ion alternations, and the peak at 0.34 $Å^{-1}$ arises from the segregation of alkyl chains and corresponds to scattering domains about 1.8 nm in size [23, 51]. With respect to peak intensity and peak width, the latter feature is equivalent to the case of the pure ionic liquid HC_8ImTFSI, indicating that the addition of imidazole does not disrupt the native structuration of the

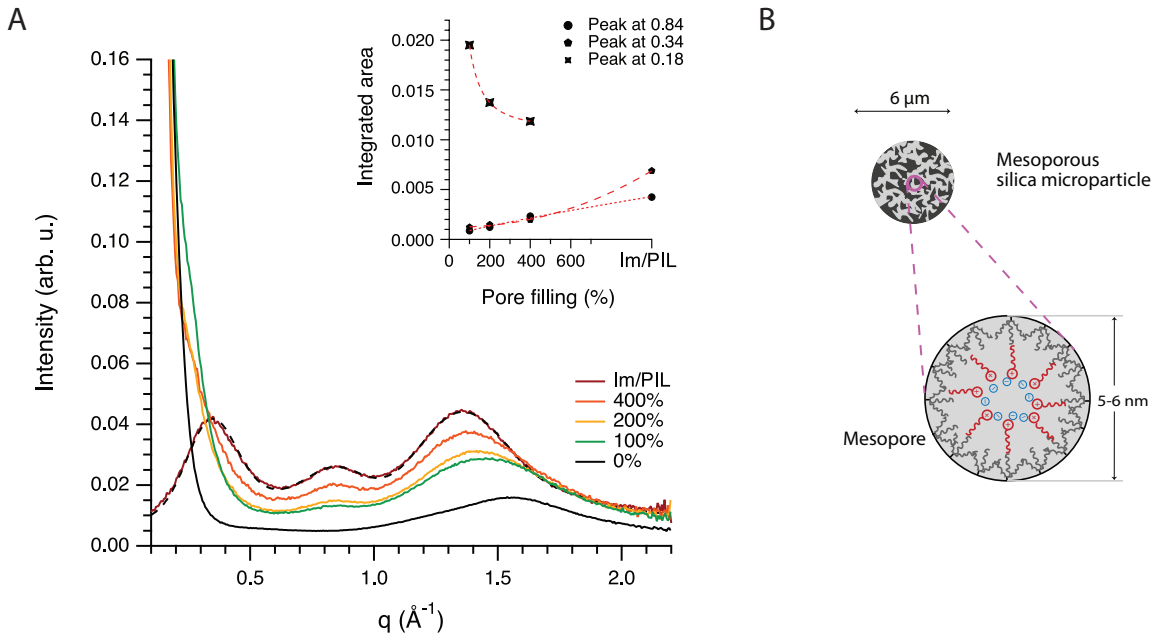

Figure 4.3: *A: Small-angle X-ray scattering intensity collected for the bare silica particles (black trace), different samples with varying pore filling (orange, yellow and green) and the neat Im/PIL mixture (dark red). The inset plot shows the integrated areas under selected fit peaks as a function of composition. B: Illustration of the speculated local structure inside the mesopores, based on X-ray observations.*

ionic liquid [23]. Furthermore, the bare silica particles contribute at about 1.6 Å^{-1} with a broader feature and with a strongly increasing scattering intensity in the low-q range (below 0.3 Å^{-1}). After multiple-peak fitting on the scattering data, it was found that the position of these peaks did not shift significantly, but the intensities of the characteristic peaks (i.e. the integrated areas under the peaks) at 0.34 Å^{-1} and 0.84 Å^{-1} increased with increased pore filling factor, see inset of Figure 4.3 A. Hence, these unchanged peak positions can indicate that the local ion-ion distances and segregation of alkyl chains are the same inside the mesopores as in the bulk liquid phase.

In the PIL/silica hybrid materials an additional feature below 0.4 Å^{-1} can be observed, which is not present in the X-ray scattering pattern of the neat 5-C8-SiO_2 silica particles and the Im/PIL mixture. After peak fitting, the centering of this feature was found to be at ∼0.18 Å for all compositions, corresponding to ∼3.5 nm real space distance. Its intensity, unlike the peaks at 0.34 Å^{-1} and 0.84 Å^{-1}, increased for decreasing filling factors, see the inset of Figure 4.3 A. Based on the X-ray scattering results, it is realistic to assume a local structure inside the mesopores with the charged centers (i.e. cation heads and TFSI anions) oriented towards the center of the pores and a looser molecular packing with a tail-to-tail separation that can match the observed repeating distance of ∼3.5 nm. A sketch of this local structure is given in Figure 4.3 B, while the hypothesized

loose packing inside the pores is here rationalized based on the high curvature of the small mesopores.

Vibrational spectroscopy was used to study interaction sensitive vibrational modes that give information on possible interactions in which the IR and Raman sensitive groups of the ionic liquid are involved, Fig. 4.4. In addition to this, chemical mapping of the PIL/silica hybrid materials with confocal Raman spectroscopy was used to confirm that the Im/PIL mixture penetrated into the pores of the mesoporous silica and distributed evenly, see Paper I. Furthermore, by having exact information on the location of the silica particles on the sample stage, Raman spectra of the PIL/silica hybrid materials was taken on the Im/PIL mixture filled silica particles, and in case of samples with pore filling of 200% and 400% also outside of them. Described in more detailed in Paper I, the Raman spectra inside and outside of the PIL/silica hybrid spectra were identical, however, an interesting phenomenon of increased Raman intensity was observed

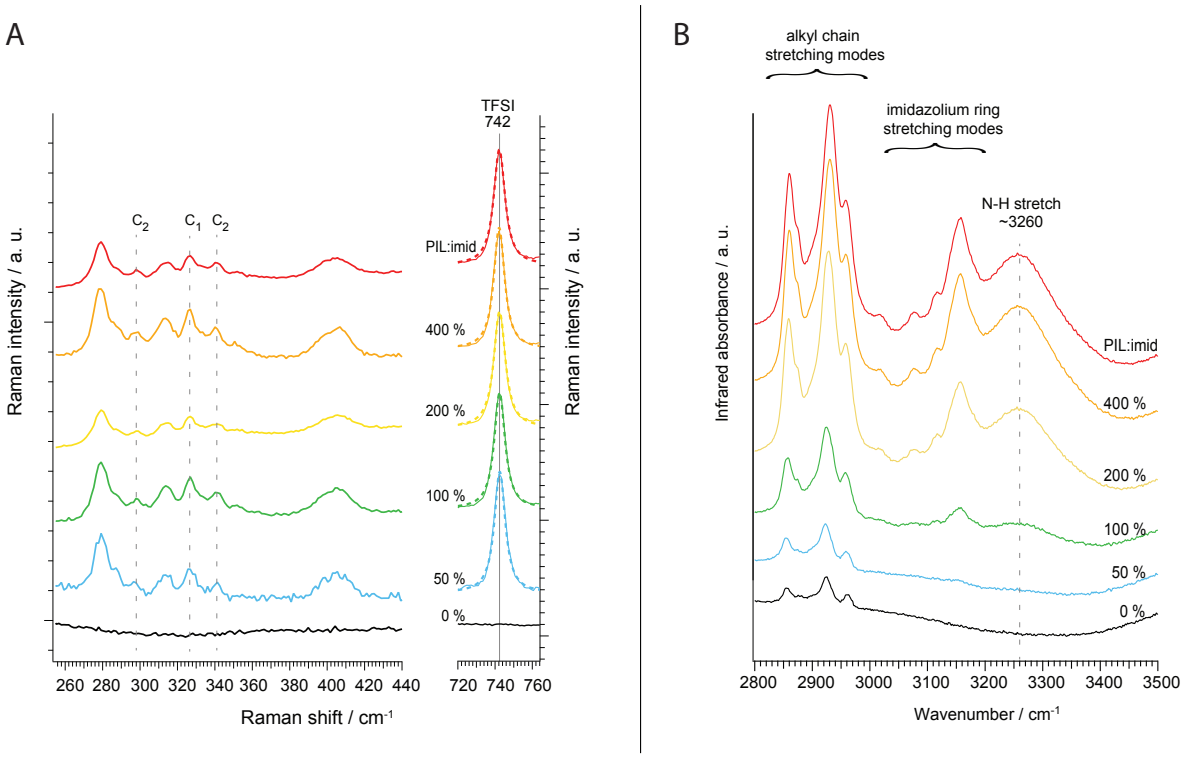

Figure 4.4: *A: Selected regions of the Raman spectra collected for the Im/PIL mixture and the mesoporous silica microparticles filled with Im/PIL mixture at various degrees of pore filling. The dashed lines show the fitting by a Lorentzian function of the range 720 - 760 cm^{-1}, where the expansion-contraction mode characteristic of the TFSI anion appears B: High frequency range of the infrared spectra collected for the Im/PIL mixture and the mesoporous silica microparticles filled with Im/PIL mixture mixture at various degrees of pore filling.*

inside of the particles. Similarly, shown on Fig. 4.4 A, the Raman spectra of the PIL/silica hybrid materials (recorded inside the particles) remain practically unchanged compared to the spectrum of the neat Im/PIL mixture.

More precisely, the Raman shift range of 240-440 cm^{-1} that contains vibrational modes associated to the two conformational states of TFSI [52, 53] and the expansion-contraction mode of TFSI at ∼742 cm^{-1} was studied. The Raman peaks associated to C_1 (*cisoid*) and the C_2 (*transoid*) remain practically unchanged upon nano-confinement, see Figure 4.4A, revealing that the conformational population of TFSI and the TFSI – imidazolium association were unchanged inside the mesopores if compared to the case of the bulk Im/PIL mixture. Furthermore, by peak fitting we found that the expansion-contraction mode at ∼742 cm^{-1} does not shift in frequency with composition and does not broaden either. These features of the Raman spectra lead to the conclusion that the TFSI anion does not interact significantly with the silica walls, which agrees with results from X-ray scattering. This is in line also with a previous study by Garaga et al. [5], which showed that due to what was called by the authors flipped-ion effect in proximity to a hydrophobized silica wall; with the alkyl chain of the imidazolium cation facing the silica wall the local interaction between the TFSI anion and the imidazolium head remain the same as in the pure PIL or the Im/PIL mixture. A different scenario is when a blue shift for the ∼742 cm^{-1} mode has been observed in the case of untreated silica that offers -SiO^- and -SiOH sites of interactions [52].

As a complement to Raman measurements, IR spectroscopy was used to study the interaction sensitive vibrations of the imidazolium cation, Figure 4.4 B, namely its alkyl chain stretching modes, imidazolium ring stretching modes, and its N-H stretch. For the samples with a pore filling equal to or higher than 200%, no shifts could be detected for any peaks with respect to the spectrum of the neat Im/PIL mixture. However, in the sample with 100% pore filling a small but measurable red shift for the broad N-H stretching mode was observed, see also Figure S2 in the ESI file of Paper I. This peak arises mainly from the imidazolium cation, with minor contributions from imidazole, and its slight red shift reflects an average increase of the N-H bond length [3].

4.2 Nanochannel formation with an ionic liquid soft-template

Mesoporous silica thin films were synthetized with electrochemically assisted self-assembly (EASA) in the presence of a long-chain aprotic imidazolium ionic liquid (IL), C_{16}MIMCl, with various IL/TEOS ratios. The thin films were studied with various methods to characterize morphology, chemical composition, and permeability that support understanding the underlying templating mechanisms.

4.2.1 Morphology

Based on morphological characterization, the formation of vertically ordered mesoporous channels running through the entire silica film thickness was observed on all silica thin films that were deposited from solutions with an IL/TEOS ratio between 0.32 and 1.60, for further details see Paper II. Electron microscopic images of the IL-templated silica thin films after extraction of the IL are shown in Fig. 4.5. In Fig. 4.5A, TEM image of the cross-sectional sample prepared with the

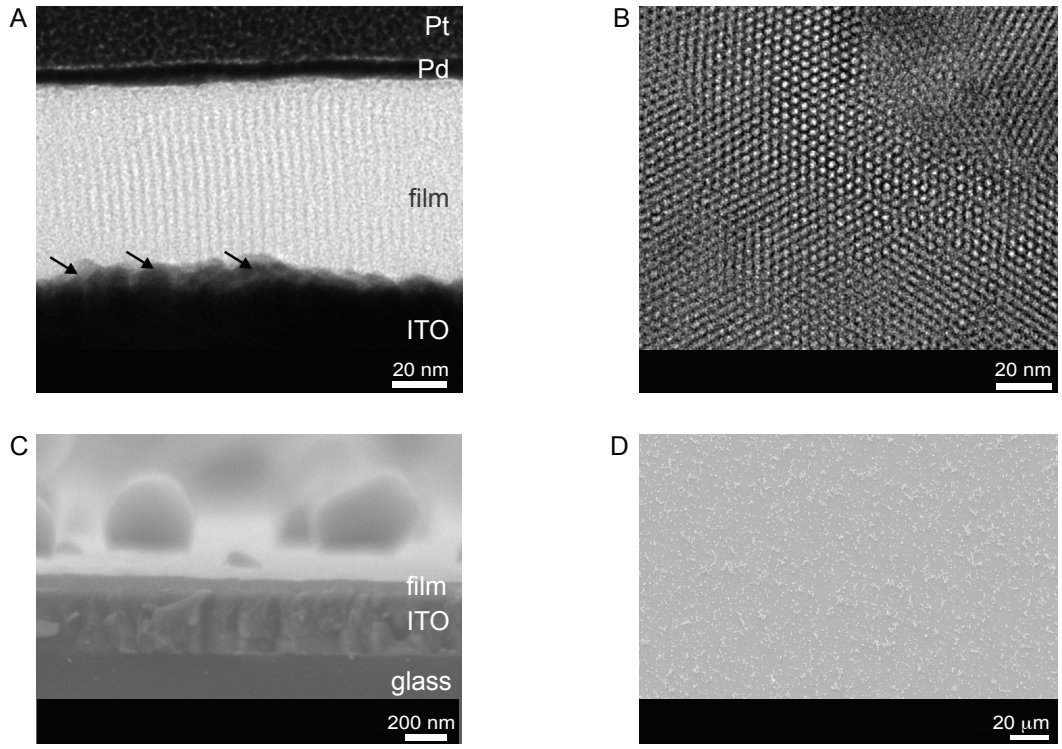

Figure 4.5: *Electron microscopic images of the IL-templated silica thin films after extraction. A: cross-sectional TEM image of a 0.32 E sample prepared with the lift-out technique. The arrows point to the interface between the thin film and ITO; B: top-view TEM image of a 0.32 E sample; C: cross-sectional SEM image of a 0.64 E sample on its substrate; D: top-view SEM image of a 0.64 E sample.*

lift-out technique is shown, revealing the local structure of the channels within the thin film. It is shown that individual channels in the silica film are straight and vertical to the ITO substrate and can reach its surface in direct contact. A complementary top view TEM image also shows that these channels are not only well-separated, but also hexagonally ordered, Fig. 4.5B. After image processing, the pore width was determined to be approximately 2.5 ± 0.3 nm. In general, channels with similar porewidth are both called mesochannels and nanochannels, here, therefore the two terms are used synonymously. Nevertheless, pore width of the channels are independent of the IL/TEOS ratio used in the deposition solutions and its size is similar to the size of two adjacent hexadecyl-tails therefore it can be assumed that the IL has a core-shell packing in the pores with the hydrocarbon tails forming the core and the charged heads forming the outer shell [23, 51].

Furthermore, based on cross sectional SEM images, the IL-templated silica thin films are shown to be deposited as even, continuous layers without any cavities between the film and the ITO substrate, Fig. 4.5C. In addition, SEM and TEM images revealed that the films' thickness is around 70 nm. Also, on the SEM images the presence of nanoparticles on top of the films can be observed, Fig. 4.5C and 4.5. These are side products of the EASA process and their presence has been described in the literature also for other EASA-prepared films [54].

Grazing-incidence X-ray scattering patterns of the IL-templated silica films were collected to study pore morphology on a macroscopic area. GISAXS results confirm that the presence of vertically oriented, hexagonally ordered pore morphology is the long-range, dominating pore structure in the films, Fig. 4.6. In fact, the highest scattering intensities originate from the vertical mesochannels resulting in characteristic peaks along the q_y scattering vector. Moreover, after processing the 2D scattering patterns with horizontal integration, Fig. 4.6 A, the intensity peaks could be assigned to the (10), (11), (20), and (21) reflections of the hexagonal lattice of the pores as the relation between the position of the scattering peaks $q_y(10) : q_y(11) : q_y(20) : q_y(21)$ is consistent with the relation $1 : \sqrt{3} : \sqrt{4} : \sqrt{7}$, which is characteristic of the hexagonal p6m symmetry [55, 56]. Furthermore, there was no significant shift in the q_y peak positions in films characterized before and after extraction, indicating that the pore morphology remains unchanged upon extraction and demonstrating the stability of the silica network. The positions of the q_y scattering vectors are independent also on the IL/TEOS ratio of the deposition solution, showing a (10) lattice spacing of ≈3.8 nm and a (11) lattice spacing of ≈2.2 nm for all IL-templated silica films.

Next to the characteristic scattering pattern along the q_y axis, there are weak-intensity rings on the 2D X-ray scattering patterns of the not-extracted samples (NE), Fig. 4.6B and Paper II. The appearance of these rings can be explained by the silica nanoparticles on the film, also seen on SEM images, having mesopores with comparable size to the mesochannels in the films. The random orientation

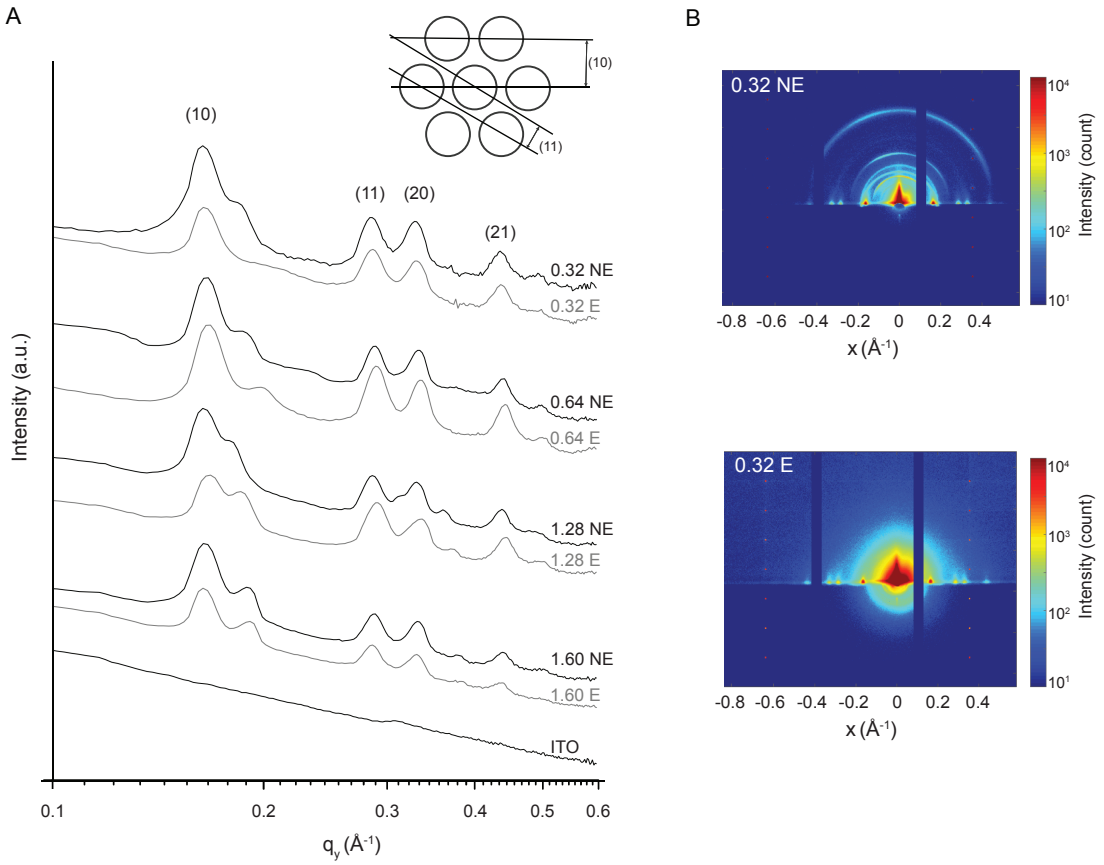

Figure 4.6: *Grazing-incidence X-ray scattering of IL-templated silica thin films. A: Horizontally integrated X-ray scattering intensities of different silica thin films. B: Selected 2D X-ray scattering patterns, i.e. for a sample before (0.32 NE, left) and after (0.32 E, right) the extraction of the IL.*

of the mesopores in the particles is shown by that they scatter X-ray also in q_z direction forming a ring shape pattern. Also, it can be seen on the 2D scattering patterns before (NE) and after extraction (E) of the IL that the intensity of the rings is lower for the extracted samples, indicating the partial removal of the particles.

4.2.2 Chemical composition and permeability

Based on elemental analysis done with XPS measurements, the chloride anion of the IL was undetectable in the silica thin films deposited from reaction solutions with IL/TEOS ratios between 0.32 and 1.28, see Table S2 in the ESI of Paper II. Besides, in the IR spectra of these samples after extraction, the ν_{O-H} ($\sim$ 3400 cm^{-1}) stretching vibration peak appears and the intensity of the ν_{Si-OH} ($\sim$ 950 cm^{-1}) stretching vibration increases, reflecting an increased abundance of silanol bonds (Si-OH) in the extracted films, see Fig. 4.7 A. Based on XPS and IR

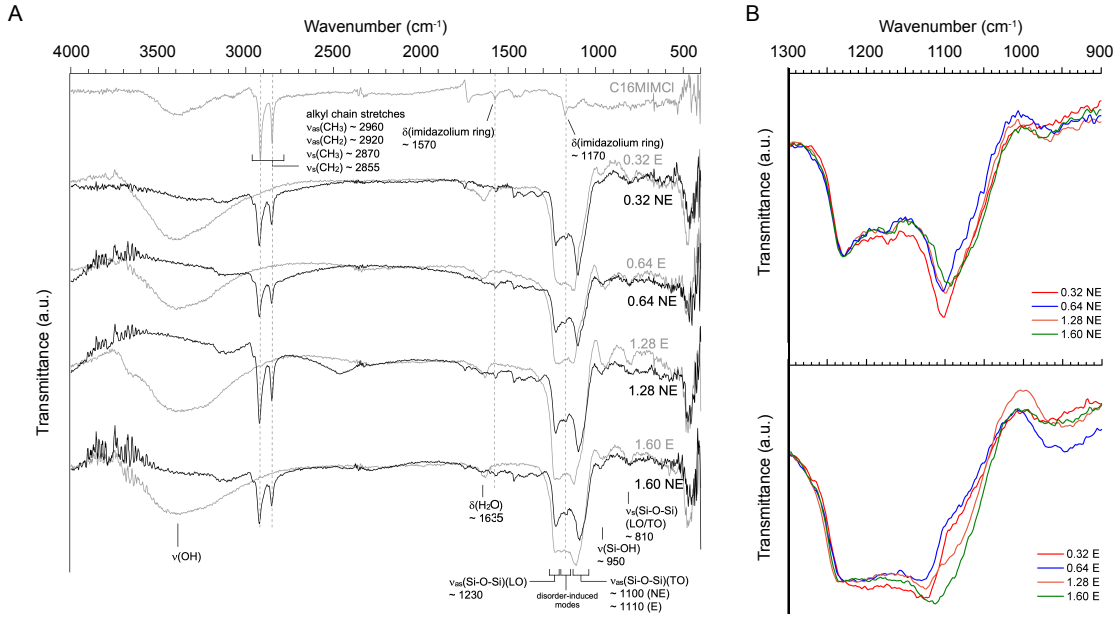

Figure 4.7: *A: Infrared spectra collected with an oblique incidence angle from the IL-templated silica thin films. B: Close up of the 1300-900 cm^{-1} region of the infrared spectra presented in A.*

results, it can be assumed that on the silica pore wall of as synthetized thin films the silanol groups are deprotonated, having their negative charges neutralized by the $C_{16}MIM^+$ cations, as schematically depicted in Fig. 4.8. These results also suggest that at the extraction step, aimed to remove the $C_{16}MIM^+$, the negatively charged silica wall gets protonated by the hydrochloric acid of the extraction solution resulting in the intensity rise of the ν_{Si-OH} peak. However, it is reasonable to assume that dangling silanol groups are located not only on the pore walls, but also in the bulk silica phase since the $\nu_{Si-OH}(\sim 950\ \text{cm}^{-1})$ stretching mode appears in both extracted and non extracted samples.

Full removal of $C_{16}MIM^+$ *via* extraction was confirmed by IR, since the alkyl chain ν_{C-H} (2960 – 2855 cm^{-1}) stretching vibrations and the imidazolium ring δ_{ring} (1570 cm^{-1}) bending vibrations disappear from the IR spectra of the ex-

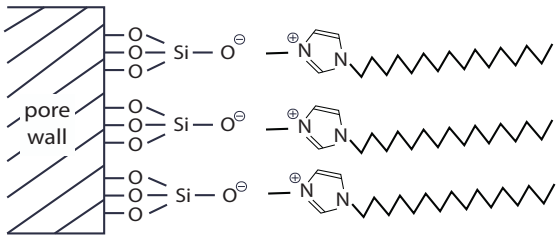

Figure 4.8: *Schematic of the proposed neutralization of the negatively charged silica wall by $C_{16}MIM^+$ cations in the mesochannels of the IL-templated silica thin films.*

tracted samples, Fig. 4.7A. From this, it follows also that the $C_{16}MIM^+$ cations are located only in the mesochannels of the films and do not get entrapped in the bulk silica network.

The amorphous structure of the deposited silica films is demonstrated by several features in their IR spectra; characteristic longitudinal-optic-transverse-optical (LO-TO) splitting of the $\rho_{Si-O-Si}$ (507 - 457 cm^{-1}), $\nu_{s(Si-O-Si)}$ (820 - 810 cm^{-1}), and the $\nu_{as(Si-O-Si)}$ (1250 - 1070 cm^{-1}) vibrational modes [57], Fig. 4.7 A and B. Both the $\nu_{as(Si-O-Si)}$(LO) and the $\nu_{as(Si-O-Si)}$(TO) modes show considerable widths indicative of a wide distribution of Si-O-Si bond angles and bond lengths. After extraction of the IL, the shift of the $\nu_{as(Si-O-Si)}$(TO) mode to higher frequencies reveals the increase in Si-O-Si bond angles in the silica network. In addition, a further feature that we observe in the amorphous silica, is the rise of a feature at ~1200 cm^{-1} between the $\nu_{as(Si-O-Si)}$ LO and TO peaks, also referred to as the "disorder-induced" mode [57]. Furthermore, the shoulder of $\nu_{as(Si-O-Si)}$(TO) at 1050 – 1100 cm^{-1} can be related to the presence of non-bridging oxygens in the network. Important to note also that water was not detected by IR in the IL-templated silica thin films before extraction (NE samples), suggesting that the included ionic liquid imparts hydrophobicity to the synthesized material.

Ion permeation through the mesochannels before and after removal of the ionic liquid was investigated by monitoring the transport properties of a redox-active electrochemical probe, here the Ru(III) cation, with cyclic voltammetry, Fig. 4.9. Cyclic voltammetric results provided information not only on the quality of the deposited films, but also supported the proposed neutralization of the negatively

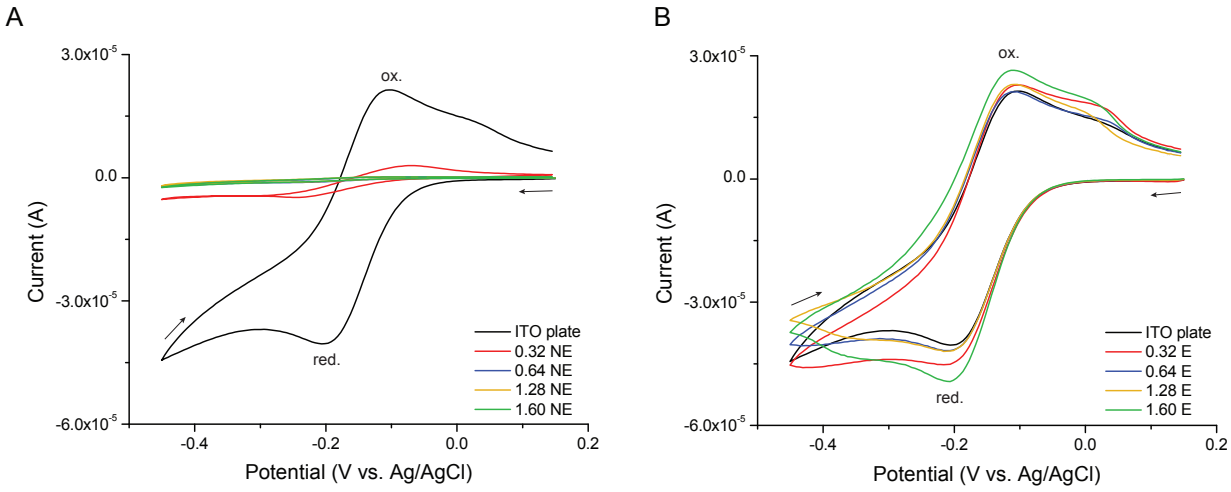

Figure 4.9: *Cyclic voltammetry curves recorded in a Ru(III) solution using a bare ITO electrode and ITO electrodes covered with the IL-templated silica thin films, before (A) and after (B) extraction of the IL.*

charged silica wall by $C_{16}MIM^+$ cations, presented on Fig. 4.8. On the voltammogram recorded with bare ITO, the negative peak current on forward scan indicates reduction of $Ru(NH_3)_6{}^{3+}$ to $Ru(NH_3)_6{}^{2+}$ and the positive peak on reversal scan corresponds to the oxidation of $Ru(NH_3)_6{}^{2+}$ to $Ru(NH_3)_6{}^{3+}$ [58], Fig. 4.9 A. As compared to the case of the bare ITO electrode, the measured currents was drastically lower when recorded on silica thin films that still contained $C_{16}MIM^+$ in its mesochannels (NE), Fig. 4.9 A. This shows that the redox reactions of the ruthenium ions are hindered due to restricted or blocked diffusion pathways through these films. For the silica thin films that were deposited from solutions with a IL/TEOS ratio of 0.64 or higher, no significant current was measured at all in the applied voltage range, behaving as insulator layers impeding the ruthenium ions to reach the electrode. When the deposition solution had a IL/TEOS ratio of 0.32, the CV curve of the silica thin film sample 0.32 NE showed a measurable current with peak positions close to the reduction and oxidation peaks measured on bare ITO; the appearance of these low current peaks can be explained by an imperfect coverage of the film on the electrode, resulting in ruthenium ions able to reach the electrode to some extent. However, the shifted peaks indicate hindered diffusion. Nevertheless, from the well-insulating behavior of the films deposited from solution with an IL/TEOS ratio of at least 0.64, two important features of the films can be described. Firstly, these insulating films have full coverage of the surface and good contact with the ITO. Secondly, the cation of the IL, $C_{16}MIM^+$, does not diffuse upon cathodic potential and $C_{16}MIM^+$ remains insoluble for the contacting aqueous solution. This shows that there is strong electrostatic attraction between the negatively charged silica wall and the $C_{16}MIM^+$ cation that prevents not only the diffusion of the $C_{16}MIM^+$ ion, but also the penetration of the Ru(III) cation through the mesochannels.

After removal of the $C_{16}MIM^+$ from the channels, the IL-templated silica thin films show drastically changed permeability properties, Fig. 4.9 B. On the cyclic voltammograms of the extracted samples both oxidation and reduction peaks of the ruthenium redox probe appeared, similar to the voltammogram recorded on bare ITO. This reveals that the ruthenium ions could reach the ITO electrode through the emptied mesochannels.

4.2.3 Possible interactions during templating

As morphological characterization revealed, the hexagonally ordered, vertically oriented, channel-like pore morphology formed by $C_{16}MIMCl$ is similar to the pore morphology of the CTAB-templated, EASA-deposited silica films, previously reported by Walcarius et al. [59, 60]. The similarity of the two amphiphiles is intriguing. It is known that the morphology of the silica films deposited with CTAB is extremely sensitive to synthesis parameters; TEOS concentration, type and amount of co-solvent, salt composition and concentration all were studied

in detail before setting them as all influence the self-assembly of CTAB both in bulk and at the surface during deposition [54]. Meanwhile, the study presented in Paper II shows that for a selected set of synthesis parameters, the use of the ionic liquid C_{16}MIMCl instead of CTAB results in the same pore morphology of the film with the only difference that a higher voltage had to be applied during EASA [56, 60]. This indicates that self-assembly of C_{16}MIMCl, and therefore supposedly also its packing parameter, is very similar to that of CTAB under the synthesis conditions of EASA and that C_{16}MIMCl can be used as templating agent for formation of mesochannel just as successfully as CTAB.

Furthermore, in-depth characterization of the film shows presence of electrostatic attraction between the pore forming $C_{16}MIM^+$ ions and the negatively charged silica pore wall, which reasonably originates from the electrostatic attraction between the $C_{16}MIM^+$ and the network-forming negatively charged silicate oligomers in line with that condensation of the silica network proceeded on basic pH. Furthermore, it can be proposed that the described electrostatic attraction is the main so-called cooperative interaction during pore formation as C_{16}MIMCl and CTAB form mesochannels with high curvature at the same range of template-to-precursor ratio in the deposition solution. This also suggests that hydrogen bonds and π-π interactions, which the aromatic imidazolium head is able to establish, remain secondary under the reaction conditions of the EASA process.

5 Conclusion and outlook

This thesis presents studies on organic-inorganic hybrid materials made of imidazolium ionic liquids and mesoporous silicas. Based on Paper I, an in-depth study was presented on an imidazole/PIL mixture confined in hydrophobized mesoporous silica particles focusing on proton transport mechanisms and correlated local structures within the pores. It has been found that the ionic conductivity in the hybrid materials on macroscopic scale is dominated by the vehicular mechanism. Nevertheless, PFG-NMR results have also shown the occurrence of proton motion decoupled from the imidazolium cation that, for issues of line broadening, could not be investigated for the samples with filling factors of 50 and 100%. For samples with higher filling factors than 100%, when the Im/PIL mixutre is in excess and located also in between the particles, both protonic and ionic mobility is enhanced, meaning that as an average behaviour has been measured, the question whether a decoupled proton motion also occurs inside the pores remains open. This study also reveals that interactions at the molecular level are practically unchanged upon confinement in hydrophobized silica mesopores as compared to the bulk case. Hence, in line with previous studies by Garaga et. al. [3], flipped-ion effect is assumed to occur and the non-polar alkyl chain of the cations to orient towards the hydrophobic silica pore wall. In such structuration there are weak cation-silica interactions that favor unrestricted diffusion, which is otherwise hindered under nano-confinement.

Possible use of ionic liquids as soft-templates for mesoporous silica synthesis was also discussed and presented based on Paper II. It extends the possibilities of templating silica with ionic liquids which is relevant in developing methods for synthesis of ionic liquid-based functional hybrid materials. In our approach, we used a long chain imidazolium ionic liquid during the EASA method to deposit mesoporous silica thin films with vertically aligned, distinct mesochannels with a well defined pore size and a highly packed hexagonal arrangement. Moreover, these mesochannels run through the entire film thickness enabling mass transport through the film and a robust contact with the substrate after removal of the templating IL. Important information on the underlying mechanism of pore formation has been gained as well; the presented study revealed electrostatic attraction between the pore forming $C_{16}MIM^+$ ions and the negatively charged silica pore wall, which reasonably originates from the electrostatic attraction between the $C_{16}MIM^+$ and the network-forming negatively charged silicate oligomers. This electrostatic attraction is proposed to be the main cooperative interaction during

pore formation, while results also indicate that hydrogen bonds and π-π interactions, which the imidazolium head is able to establish, remain secondary during synthesis.

The presented studies in this thesis inspire further research with the purpose of achieving new ionic liquid-based functional hybrid materials by applying the EASA method on PILs or mixtures of long and short chain imidazolium ionic liquids or on other yet unexplored ionic liquids structures. The concept of useing PILs for formation of the mesochannels during EASA is especially appealing considering that the vertical alignment of channels in the silica films is highly desired in applications that utilize some sort of transport phenomena within the channel-like pores i.e. proton transport., since such a structure provides shortened, oriented diffusion pathways.

6 Acknowledgements

Funding from the Swedish Foundation for Strategic Reserach (SSF, grant no FFL-15 0092), from the Knut & Alice Wallenberg Foundation (Wallenberg Academy Fellow, grant no 2016-0220) and from the Swedish Research Council (grant no 2018-05207) is greatly acknowledged.

This work was performed at the Division of Applied Chemistry and the Chalmers Material Analysis Laboratory (CMAL) in Chalmers Univerity of Technology, and Laboratorie de Chimie Physique et Microbiologie pour les Materiaux et l'Environnement, LCPME, France.

I would like to thank my supervisor, Anna Martinelli for creating a supportive and creative atmosphere.

Help and fruitful discussions with co-authors Neus Vila, Antiope Lotsari, Alain Walcarius, Khalid Elamin, Lars Nordstierna, and Anna Martinelli are greatly appreciated and acknowledged.

I would also like to thank past and current members of the Martinelli group; Olesia, Khalid, Mohammad, Iqbaal, and Eduardo. Also to friends and colleagues of the Division of Applied Chemistry. It is a pleasure to work and co-operate with so many great people.

And big, warm thanks to my family members, Tibor, Vné (Ilona), Zorán, my firends, Kata, Gergő, Pati, André, Claudia, and Gio, and of course to the kindest person I know, to my partner, Johan.

References

[1] I. Staffell, D. Scamman, A. Velazquez Abad, P. Balcombe, P. E. Dodds, P. Ekins, N. Shah and K. R. Ward, "The role of hydrogen and fuel cells in the global energy system", *Energy and Environmental Science*, 2019, **12**, 463–491 (cit. on p. 1).

[2] F. Barbir, *Fuel Cell Electrochemistry*, 2013, pp. 33–72 (cit. on pp. 1, 2).

[3] M. N. Garaga, V. Dracopoulos, U. Werner-Zwanziger, J. W. Zwanziger, M. Maréchal, M. Persson, L. Nordstierna and A. Martinelli, "A long-chain protic ionic liquid inside silica nanopores: Enhanced proton mobility due to efficient self-assembly and decoupled proton transport", *Nanoscale*, 2018, **10**, 12337–12348 (cit. on pp. 1, 4, 5, 22, 23, 27, 29, 30, 33, 41).

[4] T. Norby, "Solid-state protonic conductors: Principles, properties, progress and prospects", *Solid State Ionics*, 1999, **125**, 1–11 (cit. on p. 1).

[5] M. N. Garaga, L. Aguilera, N. Yaghini, A. Matic, M. Persson and A. Martinelli, "Achieving enhanced ionic mobility in nanoporous silica by controlled surface interactions", *Physical Chemistry Chemical Physics*, 2017, **19**, 5727–5736 (cit. on pp. 1, 4, 5, 33).

[6] M. N. Garaga, M. Persson, N. Yaghini and A. Martinelli, "Local coordination and dynamics of a protic ammonium based ionic liquid immobilized in nanoporous silica micro-particles probed by Raman and NMR spectroscopy", *Soft Matter*, 2016, **12**, 2583–2592 (cit. on pp. 1, 4).

[7] S. Zhang, J. Zhang, Y. Zhang and Y. Deng, "Nanoconfined Ionic Liquids", *Chemical Reviews*, 2017, **117**, 6755–6833 (cit. on pp. 1, 3, 4).

[8] J. Ingenmey, S. Gehrke and B. Kirchner, "How to Harvest Grotthuss Diffusion in Protic Ionic Liquid Electrolyte Systems", *ChemSusChem*, 2018, **11**, 1900–1910 (cit. on pp. 1, 4).

[9] M. Hasani, L. M. Varela and A. Martinelli, "Short-Range Order and Transport Properties in Mixtures of the Protic Ionic Liquid [C2HIm][TFSI] with Water or Imidazole", *Journal of Physical Chemistry B*, 2020, **124**, 1767–1777 (cit. on pp. 1, 4).

[10] A. S. Amarasekara, "Acidic Ionic Liquids", *Chemical Reviews*, 2016, **116**, 6133–6183 (cit. on p. 1).

[11] M. Cifelli et al., “Study of Translational Diffusion Anisotropy of Ionic Smectogens by NMR Diffusometry”, *Chemistry of Materials*, 2010, **22**, 907–925 (cit. on pp. 1, 3, 4).

[12] K. D. Kreuer, S. J. Paddison, E. Spohr and M. Schuster, “Transport in proton conductors for fuel-cell applications: Simulations, elementary reactions, and phenomenology”, *Chemical Reviews*, 2004, **104**, 4637–4678 (cit. on pp. 1, 4).

[13] J. Le Bideau, L. Viau and A. Vioux, “Ionogels, ionic liquid based hybrid materials”, *Chemical Society Reviews*, 2011, **40**, 907–925 (cit. on p. 1).

[14] J. Dupont, “From molten salts to ionic liquids: A "nano" journey”, *Accounts of Chemical Research*, 2011, **44**, 1223–1231 (cit. on pp. 3, 7).

[15] J. N. Canongia Lopes and A. A. Pádua, “Nanostructural organization in ionic liquids”, *Journal of Physical Chemistry B*, 2006, **110**, 3330–3335 (cit. on pp. 3, 7).

[16] R. E. Morris, “Ionothermal synthesis - Ionic liquids as functional solvents in the preparation of crystalline materials”, *Chemical Communications*, 2009, 2990–2998 (cit. on pp. 3, 7).

[17] N. Yaghini, V. Gómez-González, L. M. Varela and A. Martinelli, “Structural origin of proton mobility in a protic ionic liquid/imidazole mixture: Insights from computational and experimental results”, *Physical Chemistry Chemical Physics*, 2016, **18**, 23195–23206 (cit. on p. 4).

[18] C. Iacob, J. R. Sangoro, P. Papadopoulos, T. Schubert, S. Naumov, R. Valiullin, J. Kärger and F. Kremer, “Charge transport and diffusion of ionic liquids in nanoporous silica membranes”, *Physical Chemistry Chemical Physics*, 2010, **12**, 13798–13803 (cit. on pp. 4, 5).

[19] C. Iacob, J. R. Sangoro, W. K. Kipnusu, R. Valiullin, J. Kärger and F. Kremer, “Enhanced charge transport in nano-confined ionic liquids”, *Soft Matter*, 2012, **8**, 289–293 (cit. on pp. 4, 5).

[20] Y. L. Verma and R. K. Singh, “Conformational States of Ionic Liquid 1-Ethyl-3-methylimidazolium Bis(trifluoromethylsulfonyl)imide in Bulk and Confined Silica Nanopores Probed by Crystallization Kinetics Study”, *Journal of Physical Chemistry C*, 2015, **119**, 24381–24392 (cit. on p. 4).

[21] M. D. Elola and J. Rodriguez, “Ionic Mobility within Functionalized Silica Nanopores”, *Journal of Physical Chemistry C*, 2019, **123**, 3622–3633 (cit. on p. 4).

[22] R. Hayes, G. G. Warr and R. Atkin, “Structure and Nanostructure in Ionic Liquids”, *Chemical Reviews*, 2015, **115**, 6357–6426 (cit. on pp. 4, 7–9).

[23] I. Abdurrokhman, K. Elamin, O. Danyliv, M. Hasani, J. Swenson and A. Martinelli, *Protic Ionic Liquids Based on the Alkyl-Imidazolium Cation: Effect of the Alkyl Chain Length on Structure and Dynamics*, 2019 (cit. on pp. 4, 30, 31, 35).

[24] R. Ciriminna, A. Fidalgo, V. Pandarus, F. Béland, L. M. Ilharco and M. Pagliaro, "The sol-gel route to advanced silica-based materials and recent applications", *Chemical Reviews*, 2013, **113**, 6592–6620 (cit. on p. 6).

[25] C. J. Brinker and G. W. Scherer, "Particulate Sols and Gels", *Sol-Gel Science*, 1990, 234–301 (cit. on pp. 6–8).

[26] T. Montheil, J. Martinez and G. Subra, "Inorganic polymerization : an attractive route to biocompatible hybrid hydrogels", 2018, 3434–3448 (cit. on p. 7).

[27] M. Antonietti, D. Kuang, B. Smarsly and Y. Zhou, "Ionic liquids for the convenient synthesis of functional nanoparticles and other inorganic nanostructures", *Angewandte Chemie - International Edition*, 2004, **43**, 4988–4992 (cit. on pp. 7, 8).

[28] F. H. Aidoudi and R. E. Morris, "Ionothermal synthesis", *RSC Catalysis Series*, 2014, **2014-Janua**, 508–536 (cit. on p. 8).

[29] J. Łuczak, M. Paszkiewicz, A. Krukowska, A. Malankowska and A. Zaleska-Medynska, "Ionic liquids for nano- and microstructures preparation. Part 1: Properties and multifunctional role", *Advances in Colloid and Interface Science*, 2016, **230**, 13–28 (cit. on pp. 8–10).

[30] R. Dutta, S. Kundu and N. Sarkar, "Ionic liquid-induced aggregate formation and their applications", *Biophysical Reviews*, 2018, **10**, 861–871 (cit. on p. 8).

[31] H. Kaper and B. Smarsly, "Templating and phase behaviour of the long chain ionic liquid C 16mimCl", *Zeitschrift fur Physikalische Chemie*, 2006, **220**, 1455–1471 (cit. on pp. 9, 10).

[32] Y. Zhou, J. H. Schattka and M. Antonietti, "Room-temperature ionic liquids as template to monolithic mesoporous silica with wormlike pores via a sol-gel nanocasting technique", *Nano Letters*, 2004, **4**, 477–481 (cit. on p. 9).

[33] A. Vioux, L. Viau, S. Volland and J. Le Bideau, "Use of ionic liquids in sol-gel; ionogels and applications", *Comptes Rendus Chimie*, 2010, **13**, 242–255 (cit. on p. 9).

[34] T. Wang, H. Kaper, M. Antonietti and B. Smarsly, "Templating behavior of a long-chain ionic liquid in the hydrothermal synthesis of mesoporous silica", *Langmuir*, 2007, **23**, 1489–1495 (cit. on pp. 9, 10).

[35] H. Zhang and S. Liu, "Preparation of ordered mesoporous silica materials templated by ionic liquids in alkaline condition", *Journal of Porous Materials*, 2019, **26**, 1–6 (cit. on p. 9).

[36] Y. Zhou and M. Antonietti, "Preparation of highly ordered monolithic supermicroporous lamellar silica with a room-temperature ionic liquid as template via the nanocasting technique", *Advanced Materials*, 2003, **15**, 1452–1455 (cit. on p. 9).

[37] Y. Zhou and M. Antonietti, "A Series of Highly Ordered, Super-Microporous, Lamellar Silicas Prepared by Nanocasting with Ionic Liquids", *Chemistry of Materials*, 2004, **16**, 544–550 (cit. on p. 9).

[38] M. Etienne, Y. Guillemin, D. Grosso and A. Walcarius, "Electrochemical approaches for the fabrication and/or characterization of pure and hybrid templated mesoporous oxide thin films: A review", *Analytical and Bioanalytical Chemistry*, 2013, **405**, 1497–1512 (cit. on pp. 10, 11).

[39] G. Herzog, E. Sibottier, M. Etienne and A. Walcarius, "Electrochemically assisted self-assembly of ordered and functionalized mesoporous silica films: Impact of the electrode geometry and size on film formation and properties", *Faraday Discussions*, 2013, **164**, 259–273 (cit. on pp. 10, 11).

[40] M. Etienne, A. Goux, E. Sibottier and A. Walcarius, "Oriented mesoporous organosilica films on electrode: A new class of nanomaterials for sensing", *Journal of Nanoscience and Nanotechnology*, 2009, **9**, 2398–2406 (cit. on p. 11).

[41] Philip Willmott, *An introduction to synchrotron radiation : techniques and applications*, John Wiley & Sons Ltd, Chichester, 2nd (cit. on p. 14).

[42] C. S. Kumar, *X-ray and Neutron Techniques for Nanomaterials Characterization*, Springer-Verlag GmbH, Germany, Berlin, 2016 (cit. on p. 15).

[43] M. Thommes, K. Kaneko, A. V. Neimark, J. P. Olivier, F. Rodriguez-Reinoso, J. Rouquerol and K. S. Sing, "Physisorption of gases, with special reference to the evaluation of surface area and pore size distribution (IUPAC Technical Report)", *Pure and Applied Chemistry*, 2015, **87**, 1051–1069 (cit. on p. 15).

[44] P. J. d. P. Atkins, *Physical Chemistry*, W. H. Freeman and Company, New York, 9th edn., 2010 (cit. on pp. 15, 18).

[45] H. Seyama, M. Soma and B. K. Theng, *X-Ray Photoelectron Spectroscopy*, Elsevier Inc., 1st edn., 2013, vol. 5, pp. 161–176 (cit. on p. 17).

[46] N. Elgrishi, K. J. Rountree, B. D. McCarthy, E. S. Rountree, T. T. Eisenhart and J. L. Dempsey, "A Practical Beginner's Guide to Cyclic Voltammetry", *Journal of Chemical Education*, 2018, **95**, 197–206 (cit. on p. 24).

[47] P. Sippel, P. Lunkenheimer, S. Krohns, E. Thoms and A. Loidl, "Importance of liquid fragility for energy applications of ionic liquids", *Scientific Reports*, 2015, **5**, 1–8 (cit. on p. 27).

[48] A. Triolo, O. Russina, H. J. Bleif and E. Di Cola, "Nanoscale segregation in room temperature ionic liquids", *Journal of Physical Chemistry B*, 2007, **111**, 4641–4644 (cit. on p. 30).

[49] O. Russina, A. Triolo, L. Gontrani and R. Caminiti, "Mesoscopic structural heterogeneities in room-temperature ionic liquids", *Journal of Physical Chemistry Letters*, 2012, **3**, 27–33 (cit. on p. 30).

[50] A. A. Pádua, M. F. Costa Gomes and J. N. Canongia Lopes, "Molecular solutes in ionic liquids: A structural perspective", *Accounts of Chemical Research*, 2007, **40**, 1087–1096 (cit. on p. 30).

[51] A. Martinelli, M. Maréchal, Å Östlund and J. Cambedouzou, "Insights into the interplay between molecular structure and diffusional motion in 1-alkyl-3-methylimidazolium ionic liquids: A combined PFG NMR and X-ray scattering study", *Physical Chemistry Chemical Physics*, 2013, **15**, 5510–5517 (cit. on pp. 30, 35).

[52] M. Nayeri, M. T. Aronson, D. Bernin, B. F. Chmelka and A. Martinelli, "Surface effects on the structure and mobility of the ionic liquid C 6C1ImTFSI in silica gels", *Soft Matter*, 2014, **10**, 5618–5627 (cit. on p. 33).

[53] A. Martinelli, A. Matic, P. Johansson, P. Jacobsson, L. Börjesson, A. Fernicola, S. Panero, B. Scrosati and H. Ohno, "Conformational evolution of TFSI- in protic and aprotic ionic liquids", *Journal of Raman Spectroscopy*, 2011, **42**, 522–528 (cit. on p. 33).

[54] A. Goux, M. Etienne, E. Aubert, C. Lecomte, J. Ghanbaja and A. Walcarius, "Oriented mesoporous silica films obtained by electro-assisted self-assembly (EASA)", *Chemistry of Materials*, 2009, **21**, 731–741 (cit. on pp. 35, 40).

[55] J. Choi, I. Gunkel, Y. Li, Z. Sun, F. Liu, H. Kim, K. R. Carter and T. P. Russell, "Macroscopically ordered hexagonal arrays by directed self-assembly of block copolymers with minimal topographic patterns", *Nanoscale*, 2017, **9**, 14888–14896 (cit. on p. 35).

[56] Y. Guillemin, M. Etienne, E. Aubert and A. Walcarius, "Electrogeneration of highly methylated mesoporous silica thin films with vertically-aligned mesochannels and electrochemical monitoring of mass transport issues", *Journal of Materials Chemistry*, 2010, **20**, 6799–6807 (cit. on pp. 35, 40).

[57] P. Innocenzi, "Infrared spectroscopy of sol â" gel derived silica-based films : a spectra-microstructure overview", *Journal of Non-Crystalline Solids*, 2003, **316**, 309–319 (cit. on p. 38).

[58] Y. Guillemin, J. Ghanbaja, E. Aubert, M. Etienne and A. Walcarius, "Electro-assisted self-assembly of cetyltrimethylammonium-templated silica films in aqueous media: Critical effect of counteranions on the morphology and mesostructure type", *Chemistry of Materials*, 2014, **26**, 1848–1858 (cit. on p. 39).

[59] A. Walcarius, E. Sibottier, M. Etienne and J. Ghanbaja, "Electrochemically assisted self-assembly of mesoporous silica thin films", *Nature Materials*, 2007, **6**, 602–608 (cit. on p. 39).

[60] S. Ahoulou, N. Vilà, S. Pillet, D. Schaniel and A. Walcarius, "Coordination Polymers as Template for Mesoporous Silica Films: A Novel Composite Material Fe(Htrz)3@SiO2 with Remarkable Electrochemical Properties", *Chemistry of Materials*, 2019, **31**, 5796–5807 (cit. on pp. 39, 40).

Appended Papers